

1 **The Role of Midlatitude Cyclones in the Emission, Transport, Production, and**  
2 **Removal of Aerosols in the Northern Hemisphere**

3  
4 **Joseph Robinson<sup>1</sup>, Lyatt Jaeglé<sup>1</sup>, Luke D. Oman<sup>2</sup>**  
5

6 <sup>1</sup>Department of Atmospheric Sciences, University of Washington, Seattle, WA, USA

7 <sup>2</sup>Atmospheric Chemistry and Dynamics Laboratory, NASA Goddard Space Flight Center,  
8 Greenbelt, MD, USA

9  
10 Corresponding author: Joseph Robinson ([jrobin15@uw.edu](mailto:jrobin15@uw.edu))

11 **Key Points:**

- 12 • Satellite observations show 20-45% enhancement of aerosol optical depth (AOD) in the  
13 warm conveyor belt airstream of midlatitude cyclones
- 14 • A global model attributes 37% of these enhancements to sulfate, 25% to organic carbon,  
15 15% to dust, and 15% to sea salt aerosol
- 16 • Midlatitude cyclones lead to 355 Tg yr<sup>-1</sup> of sea salt aerosol emissions, or 60% of the total  
17 over the northern hemisphere oceans
- 18  
19  
20  
21  
22  
23  
24  
25  
26  
27  
28  
29  
30  
31  
32  
33  
34  
35  
36  
37

## 38 **Abstract**

39 We examine the distribution of aerosol optical depth (AOD) across 27,707 northern hemisphere  
40 (NH) midlatitude cyclones for 2005-2018 using retrievals from the Moderate Resolution  
41 Spectroradiometer (MODIS) sensor on the Aqua satellite. Cyclone-centered composites show  
42 AOD enhancements of 20-45% relative to background conditions in the warm conveyor belt  
43 (WCB) airstream. Fine mode AOD (fAOD) accounts for 68% of this enhancement annually.  
44 Relative to background conditions, coarse mode AOD (cAOD) is enhanced by more than a factor  
45 of two near the center of the composite cyclone, co-located with high surface wind speeds.  
46 Within the WCB, MODIS AOD maximizes in spring, with a secondary maximum in summer.  
47 Cyclone-centered composites of AOD from the Modern Era Retrospective analysis for Research  
48 and Applications, version 2 Global Modeling Initiative (M2GMI) simulation reproduce the  
49 magnitude and seasonality of the MODIS AOD composites and enhancements. M2GMI  
50 simulations show that the AOD enhancement in the WCB is dominated by sulfate (37%) and  
51 organic aerosol (25%), with dust and sea salt each accounting for 15%. MODIS and M2GMI  
52 AOD are 60% larger in North Pacific WCBs compared to North Atlantic WCBs and show a  
53 strong relationship with anthropogenic pollution. We infer that NH midlatitude cyclones account  
54 for 355 Tg yr<sup>-1</sup> of sea salt aerosol emissions annually, or 60% of the 30-80°N total. We find that  
55 deposition within WCBs is responsible for up to 35% of the total aerosol deposition over the NH  
56 ocean basins. Furthermore, the cloudy environment of WCBs leads to efficient secondary sulfate  
57 production.

## 58 **Plain Language Summary**

59 Largescale storms occur during all seasons in the northern hemisphere midlatitudes and are  
60 responsible for a significant fraction of observed midlatitude precipitation. The meteorological  
61 environment of these cyclones influences the direct emission, removal, chemistry, and transport  
62 of aerosols. This study combines satellite observations and a global computer simulation to probe  
63 each of these processes. To do so, cyclone-centered composites are generated by averaging  
64 together 27,707 individual northern hemisphere cyclone cases between 2005-2018. Results show  
65 that the total column amount of aerosol within the rain-producing part of cyclones is enhanced  
66 and that most of this enhancement is in the form of smaller aerosol particles more likely  
67 associated with human activities. Cyclone region and season play a large role in the abundance  
68 of aerosol, with springtime cyclones downwind of Asia displaying the largest abundances. We  
69 find that strong winds within cyclones account for over half of the annual direct emission of sea  
70 salt aerosol over the northern hemisphere oceans. Furthermore, we show that midlatitude  
71 cyclones efficiently remove aerosol, accounting for 27-33% of the total over the northern  
72 hemisphere ocean basins. They also account for 27% of secondary production of sulfate and  
73 facilitate aerosol transport.

## 74 **1 Introduction**

75 Tropospheric aerosols exert considerable influence on earth's climate, ecosystems, and  
76 human health. Aerosols substantially perturb Earth's radiation balance both directly by scattering  
77 and absorbing solar radiation and indirectly by altering cloud properties (Myhre et al., 2013;  
78 Partanen et al., 2018; Shindell et al., 2013; Smith & Bond, 2014; Westervelt et al., 2015).  
79 Nutrients in the form of iron and nitrate aerosols are transported from land and deposited into  
80 ocean environments where they can promote primary production (Baker et al., 2003; Jickells &

81 Spokes, 2001). Exposure to increased levels of fine particulate matter has also been shown to  
82 result in as many as 4.2 million premature deaths each year globally (Fang et al., 2013; Silva et  
83 al., 2017).

84  
85 Explaining the full spectrum of aerosol emissions, aerosol secondary formation via  
86 oxidation of precursor gases, transport, and removal pathways has therefore been the subject of  
87 continual research in recent decades (Alfaro & Gomes, 2001; Andreae & Crutzen, 1997; Graedel  
88 & Weschler, 1981; Jacobson & Hansson, 2000; Kerminen et al., 2005; Prather, et al., 2008).  
89 Despite these efforts, large uncertainties remain in our understanding of these aerosol processes  
90 and their representation in models (Guibert et al., 2005; Hodzic et al., 2016; Kinne et al., 2003;  
91 Real et al., 2010; Q. Yang et al., 2015).

92  
93 Midlatitude cyclones are at the intersection of processes controlling the regional and  
94 global distribution of tropospheric aerosols. The ability of their warm conveyor belts (WCBs) to  
95 lift air masses into the free troposphere and redistribute them globally is a dominant pathway for  
96 the export of pollution from Asia and North America (Hannan et al., 2003; Jaffe et al., 2003;  
97 Liang et al., 2004; Sinclair et al., 2008). Research in recent decades has tried to better  
98 characterize the timing and extent of this export as well as its impact on downwind regions (e.g.,  
99 Ding et al., 2009; Eguchi et al., 2009; Luan & Jaeglé, 2013; Y. Yang et al., 2015; Yu et al.,  
100 2008). For example, Yu et al. (2008) used monthly satellite observations of aerosol optical depth  
101 (AOD) during a 4-year period to estimate 18 Tg of pollution aerosol is exported from the Asian  
102 continent each year. Luan & Jaeglé (2013) used daily satellite observations and a chemical  
103 transport model to examine aerosol transport off both Asia and North America, finding AOD to  
104 be enhanced by more than 50% during export events. Precipitation associated with midlatitude  
105 cyclones can act to remove soluble aerosols and their precursors (Park et al., 2005). Extensive  
106 cloud cover also provides a favorable environment for aerosol formation via aqueous sulfur  
107 dioxide (SO<sub>2</sub>) oxidation and growth during subsequent transport (Brock et al., 2004; Dunlea et  
108 al., 2009). Lastly, strong surface winds within the cyclone can result in enhanced sea spray  
109 emissions over oceans (Grandey et al., 2011).

110  
111 There has also been recent interest in quantifying the extent to which aerosols themselves  
112 influence midlatitude cyclones through their effects on clouds and precipitation (e.g., McCoy et  
113 al., 2018; Naud et al., 2017). McCoy et al. (2018) showed that aerosol-cloud interactions result in  
114 an increase in cloud liquid water content, overall cloud coverage, and albedo in midlatitude  
115 cyclones in both hemispheres. In addition, a strengthening of midlatitude cyclones in the North  
116 Pacific due to the increased abundance of aerosols over the pre-industrial period has either been  
117 predicted by modeling studies (Joos et al., 2017; Wang et al., 2014) or observed as increases in  
118 precipitation and the frequency of high clouds (Zhang et al., 2007). For example, Wang et al.  
119 (2014) used a multi-scale modeling approach to find precipitation is enhanced by 7-20% in North  
120 Pacific winter-time cyclones that occur under a predominantly polluted versus marine aerosol  
121 scenario.

122  
123 Transport mediated by midlatitude cyclones occurs primarily along two coherent  
124 airstreams: the WCB and dry intrusion (DI). The WCB is the major ascending airstream of  
125 midlatitude cyclones (Browning & Roberts, 1994); it originates in the warm sector of the cyclone  
126 out ahead of the cold front and rapidly ascends moist isentropically from the boundary layer to

127 the middle and upper troposphere as it travels poleward (Eckhardt et al., 2004; Stohl, 2001).  
128 Lifting of warm, moist air in the WCB results in widespread cloud cover and intense  
129 precipitation that culminates in a hallmark comma-shaped structure (Catto et al., 2010; Whitaker  
130 et al., 1988). In the upper troposphere, the WCB can turn anticyclonically in the stronger  
131 westerly flow or turn cyclonically and become aligned vertically with the surface low (Whitaker  
132 et al., 1988). Conversely, the DI originates in the upper troposphere or lower stratosphere and  
133 descends while fanning out behind the surface cold front. Downward transport of cold, dry air  
134 leads to little cloud cover and the presence of the “dry slot” as viewed on true color satellite  
135 imagery (Browning, 1997).

136  
137 In the present study, our aim is to systematically examine the processes affecting AOD  
138 distributions within northern hemisphere (NH) midlatitude cyclones. The primary tool we use to  
139 accomplish this aim is cyclone-centered compositing across 27,707 midlatitude cyclones over a  
140 14-year period (2005-2018). We composite these individual cyclones to analyze AOD as  
141 observed by the Moderate Resolution Imaging Spectroradiometer (MODIS) aboard the NASA  
142 Aqua satellite. We compare the resulting AOD composites to simulations from the NASA  
143 Modern Era Retrospective analysis for Research and Applications, version 2 Global Modeling  
144 Initiative (M2GMI) global chemistry climate model and use these simulations to interpret the  
145 observed structures in the AOD composites.

146  
147 Grandey et al. (2011) generated midlatitude cyclone composites of satellite AOD and  
148 showed a strong positive relationship between AOD and surface wind speeds within the cyclone,  
149 consistent with wind-speed dependent emissions of sea salt aerosol (SSA). In a separate analysis,  
150 Grandey et al. (2013) found a positive relationship between cloud coverage and AOD in North  
151 Atlantic cyclones, but a negative relationship between AOD and cloud top temperature. They  
152 concluded that storm structure and strength could only explain a small fraction of these  
153 relationships and that aerosol-cloud interactions were likely part of the cause. Naud et al. (2016)  
154 examined the distribution of MODIS AOD using composites of midlatitude cyclones over the  
155 NH oceans. They also found a positive relationship between AOD and cloud cover in NH  
156 midlatitude cyclones and noted that the largest AOD values often occur along frontal boundaries  
157 within the cyclone domain where precipitating clouds form.

158  
159 We build upon these previous studies by quantifying the extent to which the midlatitude  
160 cyclone environment induces aerosol vertical transport, scavenging, in-cloud oxidation of aerosol  
161 precursors, hygroscopic growth, emission of SSA, and ultimately results in aerosol export to the  
162 global atmosphere.

163  
164 In section 2 we describe the observations and models used in our analysis. We present  
165 our cyclone identification methodology and compositing approach in section 3. In section 4 we  
166 analyze AOD composites obtained from MODIS observations and M2GMI simulations and  
167 examine the seasonal variation of AOD within cyclone WCBs. In section 5 we use vertical  
168 profiles of aerosol extinction from M2GMI to examine how enhancements vary throughout the  
169 troposphere. In section 6 we use M2GMI to quantify the contributions of midlatitude cyclones to  
170 SSA emissions and aerosol budgets over the NH oceans before summarizing in section 7.

171

## 172 2 Observations and Models

### 173 2.1 MODIS AOD Observations

174 We use AOD retrievals from the MODIS instrument onboard the NASA Aqua satellite  
175 (Remer et al., 2005). Aqua orbits at an altitude of 705 km with a 16 day repeat cycle and an  
176 equatorial crossing local time of 13:30. MODIS measures reflected solar radiation and emitted  
177 thermal radiation in 36 spectral channels, six of which are used to conduct aerosol retrievals  
178 (Levy et al., 2013; Remer et al., 2005, 2008). The 2,330 km swath of MODIS provides near daily  
179 global coverage. We use the combined quality controlled 550 nm AOD (dataset  
180 “Aerosol\_Optical\_Depth\_Land\_Ocean\_Mean”) from the collection 6.1 level 3 MODIS  
181 atmosphere daily global product (MxD08\_D3; Levy et al., 2013; Wei et al., 2019a). These level  
182 3 data are gridded  $1^\circ \times 1^\circ$  AODs obtained from the level 2 instantaneous products (Platnick et al.,  
183 2015). The dataset is built from the combined ocean (best) and land (corrected) retrievals which  
184 only contains AOD for filtered retrievals over dark targets. In particular, it includes Dark Target  
185 (Levy et al., 2013) ocean retrievals having quality assurance  $\geq 1$  and Dark Target land retrievals  
186 having quality assurance equal to 3.

187

188 We also use MODIS fine mode AOD (fAOD), which is available only over oceans  
189 (dataset “Aerosol\_Optical\_Depth\_Small\_Ocean\_Mean”). MODIS assumes nine tropospheric  
190 aerosol models with varying sizes (Levy et al., 2003). These include four fine modes (effective  
191 radii 0.10, 0.15, 0.20, and 0.25  $\mu\text{m}$ ), which together account for fAOD, and five coarse modes:  
192 three for sea salt (effective radii 1.00, 1.50, 2.00  $\mu\text{m}$ ) and two for mineral dust (effective radii  
193 1.50 and 2.50  $\mu\text{m}$ ). We refer to the sum of the five coarse modes as coarse mode AOD (cAOD).

194

195 Prior to retrieving AOD, MODIS reflectances are cloud cleared at spatial resolution of  
196 500 m. The cloud-free reflectances are averaged in  $10 \text{ km} \times 10 \text{ km}$  pixels if at least 10 out of 400  
197 are available. Because of this, MODIS can retrieve AOD even if a  $10 \text{ km}$  scene is not entirely  
198 cloud free. Beginning with MODIS collection 6 this procedure uses an updated cloud masking  
199 routine to alleviate a known issue where AOD was a factor of two too large in scenes with cloud  
200 cover  $>80\%$  (Remer et al., 2008). We conduct additional filtering of the MODIS AOD for any  
201 potential remaining cloud contamination by discarding  $1^\circ \times 1^\circ$  grid cells with cloud fraction (CF)  
202 exceeding 50%. This results in the removal of  $\sim 60\%$  of the global  $1^\circ$  grid cells.

### 203 2.2 Reanalysis and Model Datasets

204 In order to identify midlatitude cyclone centers we use sea-level pressure (SLP) from the  
205 NASA Modern Era Retrospective analysis for Research and Applications, version 2 (MERRA-2;  
206 Gelaro et al., 2017). MERRA-2 is the latest NASA reanalysis and is improved over its  
207 predecessor, MERRA, as a result of updates to the atmospheric general circulation model  
208 (Molod et al., 2015) and observing system (McCarty et al., 2016). MERRA-2 has a horizontal  
209 resolution of  $0.5^\circ$  latitude  $\times$   $0.625^\circ$  longitude and 72 vertical levels extending from the surface to  
210 0.01 hPa. The SLP field used to create the midlatitude cyclone database for this study comes  
211 from the MERRA-2 assimilated meteorology product (GMAO, 2015). We average the SLP from  
212 its original 3-hourly temporal resolution and use daily means.

213

214 The M2GMI simulation is a combination of the Goddard Earth Observing System  
215 (GEOS), version 5 general circulation model (Molod et al., 2015) and the Global Modeling

216 Initiative chemistry mechanism (Duncan et al., 2007; Strahan et al., 2007). It is constrained by  
217 MERRA-2 meteorology (winds, temperature, and pressure) through a replay technique (Orbe et  
218 al., 2017). M2GMI has the same resolution as MERRA-2 ( $0.5^\circ \times 0.625^\circ$ , 72 vertical levels) and  
219 currently covers the period of 1980-2019. Fossil fuel and biofuel emissions in M2GMI come  
220 from the MACCity Inventory (Granier et al., 2011) until 2010 while more recent years are scaled  
221 up following Representative Concentration Pathways (RCP 8.5) emissions. Full descriptions of  
222 the M2GMI simulation are provided in Nielsen et al. (2017) and Strode et al. (2019). M2GMI  
223 also includes a suite of idealized tracers. In this work, we use the 25-day anthropogenic carbon  
224 monoxide tracer (hereafter AnthroCO<sub>25d</sub>). AnthroCO<sub>25d</sub> has emissions corresponding to  
225 anthropogenic CO but undergoes decay at an idealized, fixed time of 25 days.  
226

227 M2GMI is interactively coupled to the Goddard Chemistry and Aerosol Transport  
228 (GOCART) module for aerosols. GOCART simulates the major tropospheric aerosols of sulfate,  
229 black carbon, organic carbon (OC), dust, and SSA and was initially described by Chin et al.  
230 (2002) and Ginoux et al. (2001). Nitrate was added as described in Bian et al. (2017). A  
231 complete description of aerosol emissions and treatment in GOCART has more recently been  
232 given in Chin et al. (2009) and Colarco et al. (2010). SSA emissions have been modified from  
233 the original Gong (2003) formulation by re-calibration to surface friction velocity and inclusion  
234 of a sea-surface temperature dependence (Jaeglé et al., 2011) as described in Randles et al.  
235 (2017). There are five size bins for SSA corresponding to radii of 0.03-0.1, 0.1-0.5, 0.5-1.5, 1.5-  
236 5.0, and 5.0-10.0  $\mu\text{m}$ . Dust emissions are a function of the surface characteristics and wind speed  
237 following Ginoux et al. (2001). Dust is also represented by five size bins corresponding to radii  
238 of 0.1-1.0, 1.0-1.8, 1.8-3.0, 3.0-6.0, and 6.0-10.0  $\mu\text{m}$ . Sulfate and carbonaceous species have  
239 primary emissions from fossil fuel and biofuel combustion, biomass burning, as well as biogenic  
240 sources for OC. Sulfate is also produced by oxidation of SO<sub>2</sub> and dimethyl sulfide (DMS). Loss  
241 processes for each species include dry deposition, large-scale wet removal, and convective  
242 scavenging. We do note that while emissions in M2GMI are similar to those in the MERRA-2  
243 aerosol reanalysis (Randles et al., 2017), M2GMI does not constrain total AOD through the  
244 assimilation of satellite AOD and thus serves as an independent dataset with which to probe  
245 aerosol export.  
246

247 The original SSA emissions in M2GMI (8,934 Tg yr<sup>-1</sup>, 2005-2018) are similar to those  
248 used in MERRA-2 (9,318 Tg yr<sup>-1</sup>, 2000-2014; Randles et al., 2017), but more than a factor of 2  
249 larger than the recent analysis of Bian et al. (2019) (4,015 Tg yr<sup>-1</sup>) who used the NASA GEOS  
250 model with the GOCART module. The SSA GOCART emission scheme and meteorology are  
251 the same for these three simulations, however Bian et al. (2019) used a global scaling factor of  
252 0.4, while MERRA-2 and M2GMI use a scaling factor of 0.875. Bian et al. (2019) showed good  
253 agreement of their simulations with comparisons to aircraft observations of aerosol mass  
254 concentrations as well as AOD from AERONET and MODIS. We thus scale SSA emissions,  
255 mass concentrations, and AOD in M2GMI by a factor of 0.46 (=0.4/0.875). The resulting SSA  
256 emissions are 4,060 Tg yr<sup>-1</sup>, consistent with a number of the estimates reviewed in Weng et al.  
257 (2020). As aerosols are assumed to be externally mixed in GOCART, this scaling does not  
258 impact the other aerosol species simulated.  
259

260 Aerosol optical properties in GOCART are from the Optical Properties of Aerosols and  
261 Clouds (OPAC; Hess, et al., 1998; Koepke et al., 1997). Dust is assumed to be non-hygroscopic

262 while the other species undergo varying degrees of growth at higher relative humidity (see  
263 Figure 2 in Chin et al., 2002). The AOD is calculated as  $\tau = \beta M_d$ , where  $\beta$  is the mass  
264 extinction efficiency (in  $\text{m}^2 \text{g}^{-1}$ ) and  $M_d$  is the dry aerosol mass loading (in  $\text{g m}^{-2}$ ). The mass  
265 extinction efficiency is a function of the aerosol refractive indices, size distribution, particle  
266 density, and relative humidity; it is assumed to be maximum at a relative humidity of 99%.  
267 Aerosol mass concentrations and AOD from GOCART simulations have been extensively  
268 validated against both ground-based and satellite observations (Chin et al., 2002, 2009, 2014;  
269 Colarco et al., 2010; Nowottnick et al., 2010).

270  
271 To compare M2GMI against MODIS, the hourly M2GMI AOD and fAOD (sum of  
272 sulfate, organic carbon, black carbon as well SSA, dust, and nitrate with radii less than  $1.0 \mu\text{m}$ )  
273 are linearly interpolated in time to 2pm local (i.e., near the Aqua equatorial crossing time). In  
274 addition, we sample daily-averaged aerosol properties from M2GMI. Finally, we sample daily-  
275 averaged meteorological fields from M2GMI in order to examine the WCB and broader  
276 midlatitude cyclone environment.

### 277 **3 Compositing Methodology**

278 Many recent analyses have utilized composites built from fields sampled in a cyclone-  
279 centered reference frame (e.g., Booth, et al., 2018; Field & Wood, 2007; Grandey et al., 2011,  
280 2013; McCoy et al., 2018; Naud et al., 2017, 2019). Although compositing hides the variability  
281 on a cyclone-by-cyclone basis, averaging across many cases enables common patterns associated  
282 with cyclone airstreams to emerge. Midlatitude cyclone composites in turn make it possible to  
283 study meteorological and chemical signatures, and their spatiotemporal variability, in a more  
284 general framework. Further, it provides a framework for testing whether these signatures are  
285 accurately captured by global models. The composites of Knowland et al. (2015) highlighted that  
286 the WCB of strong NH midlatitude cyclones tends to enhance CO and deplete ozone ( $\text{O}_3$ ) in the  
287 middle and upper troposphere as it redistributes air from near the surface. Jaeglé et al. (2017)  
288 used cyclone-centered composites to quantify the stratosphere-to-troposphere (STT)  $\text{O}_3$  flux  
289 associated with midlatitude cyclones, finding that DIs account for 42% of the NH extratropical  
290  $\text{O}_3$  STT flux.

291  
292 In this study, we use an approach that (1) identifies NH midlatitude cyclones; (2) samples  
293 satellite/model meteorological and aerosol fields on a  $4,000 \text{ km} \times 4,000 \text{ km}$  cyclone-centered  
294 grid; and (3) generates composites and examines anomalies relative to similarly sampled  
295 background conditions.

#### 296 **3.1 NH Midlatitude Cyclone Identification**

297 We use the method described by Patoux et al. (2009) to identify NH midlatitude cyclone  
298 centers in the daily-averaged MERRA-2 SLP field. In brief, a cyclone center is identified if: (1)  
299 the grid cell is a true local pressure minimum; (2) the pressure is at least 1 hPa less than the  
300 pressure averaged over the surrounding grid cells up to  $\pm 4$  indices; (3) the Laplacian of pressure  
301 averaged over the same grid cells is at least  $0.5 \times 10^{-10} \text{ hPa m}^{-2}$ . When two or more centers are  
302 identified within 2,000 km of each other, we only select the center with the lowest central SLP.  
303 Cyclone centers are also filtered for  $\text{SLP} \leq 1,010 \text{ hPa}$  to focus our analysis on mature cyclones  
304 most likely to have a coherent WCB airstream and therefore stronger transport. Our approach is

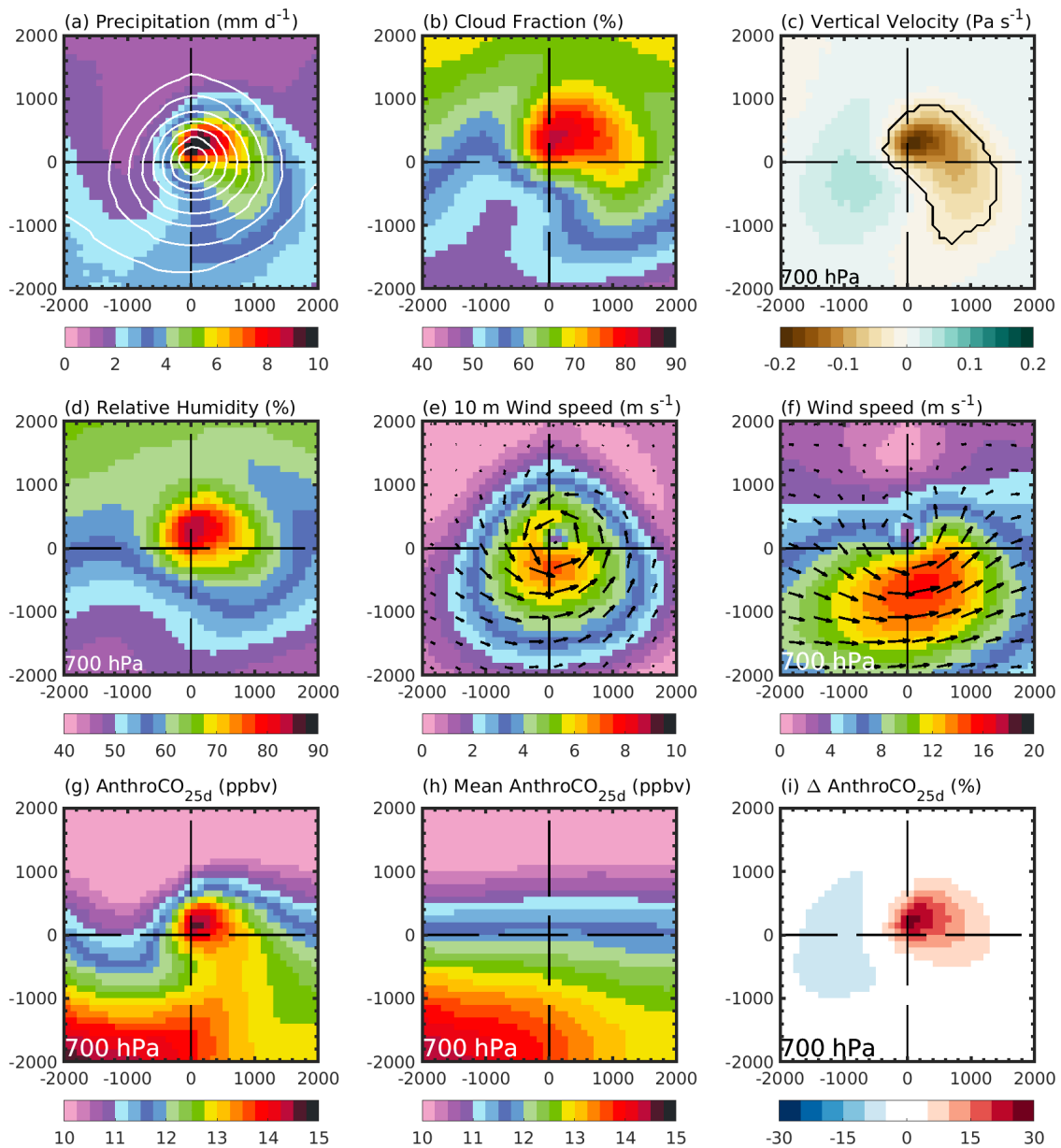
305 conducted in a Eulerian framework and does not track the position of individual cyclones during  
306 their life cycle.

307  
308 For the 2005-2018 period, we identify 27,707 midlatitude cyclones with centers between  
309 30-80° N. These midlatitude cyclones are relatively evenly distributed by season, with 29% of  
310 cyclones occurring in spring (March-April-May; MAM), 20% in summer (June-July-August;  
311 JJA), 25% in fall (September-October-November; SON), and 26% in winter (December-January-  
312 February; DJF). The spatial distribution of midlatitude cyclones shows high occurrence  
313 frequency in the North Atlantic and North Pacific storm tracks (Figure S1), consistent with  
314 previous studies (e.g., Hoskins & Hodges, 2002; Ulbrich et al., 2009; Wernli & Schwierz, 2006).

### 315 3.2 Sampling and Compositing Approach

316 We conduct cyclone-centered sampling of the MODIS and M2GMI fields at a resolution  
317 of 1°. For M2GMI, we first regrid the fields from the native 0.5° × 0.625° grid to the 1° × 1°  
318 MODIS grid. For each cyclone we use bilinear interpolation to translate and regrid the daily  
319 fields onto a 4,000 km × 4,000 km region centered over the cyclone (Field & Wood, 2007). The  
320 cyclone-centered grid has 100 km horizontal grid spacing. We then average together the cyclones  
321 to generate annual and seasonal composites. For comparison to MODIS, the 2pm local time  
322 M2GMI AOD fields are sampled when there are valid 1° × 1° MODIS retrievals and MODIS CF  
323 <50%. The same compositing is applied to 24-hour daily mean M2GMI meteorological and  
324 aerosol fields without any filtering for clouds.

325  
326 To examine how each midlatitude cyclone perturbs the distribution of aerosols relative to  
327 background conditions we generate a separate cyclone-centered grid at the same date and  
328 location of the original cyclone but instead using a 60-day running mean of each field smoothed  
329 with a 6° wide boxcar average. Anomalies (e.g.,  $\Delta\text{AOD}$ ) are given as the difference between the  
330 cyclone and its background ( $\Delta\text{AOD} = \text{AOD}_{\text{cyclone}} - \text{AOD}_{\text{background}}$ ) or as the percent enhancement  
331 relative to background ( $\Delta\text{AOD} = 100 \times (\text{AOD}_{\text{cyclone}} - \text{AOD}_{\text{background}}) / \text{AOD}_{\text{background}}$ ).



332  
 333 **Figure 1.** Annual mean composites of 27,707 midlatitude cyclones from M2GMI (2005-2018). (a) precipitation  
 334 ( $\text{mm d}^{-1}$ ), with sea-level pressure contours in white; (b) total cloud fraction (CF, %); (c) 700 hPa vertical velocity ( $\omega$ ,  
 335  $\text{Pa s}^{-1}$ ); the black contour corresponds to the mean position of the WCB airstream; (d) 700 hPa relative humidity  
 336 (%); (e) 10 m wind speed ( $u_{10m}$ ,  $\text{m s}^{-1}$ ), with vector winds represented by arrows; (f) 700 hPa wind speed ( $\text{m s}^{-1}$ ),  
 337 with vector winds represented by arrows; (g) 700 hPa  $\text{AnthroCO}_{25d}$  (ppbv); (h) Background 700 hPa  $\text{AnthroCO}_{25d}$   
 338 (ppbv); (i) 700 hPa  $\text{AnthroCO}_{25d}$  anomaly. For each panel, the  $x$  and  $y$  axes labels represent the distance from the  
 339 cyclone center ( $x = 0$  and  $y = 0$ ) in kilometers, with  $x$  increasing in the eastward direction and  $y$  increasing in the  
 340 poleward direction.

341

342

343 Figure 1 shows the annual mean 2005-2018 NH midlatitude cyclone composites of  
 344 M2GMI precipitation, CF, vertical velocity ( $\omega$ ) at 700 hPa, relative humidity (RH) at 700 hPa,  
 345 10 m wind speed ( $u_{10m}$ ), and wind speed at 700 hPa. Maximum precipitation ( $>8 \text{ mm d}^{-1}$ ) occurs  
 near the center of the cyclone and curves to the southwest to create the characteristic comma

346 shape (e.g., Field & Wood, 2007; Naud et al., 2017; Figure 1a). Strongest ascent (minimum  $\omega$ )  
347 associated with the WCB also occurs near the center of the cyclone co-located with the region of  
348 precipitation. In this region of the composite,  $\omega$  values of  $-0.2 \text{ Pa s}^{-1}$  represent about 175 hPa of  
349 overall ascent extrapolated to a 24-hour period (Figure 1c). The most extensive CF (>75%) in the  
350 composite occurs where the WCB turns cyclonically and creates the “cloud head” as viewed in  
351 satellite imagery (Catto et al., 2010; Figure 1b). The air at 700 hPa has high RH (>80%) near the  
352 center of the composite (Figure 1d). The flow near the surface is cyclonic, with  $u_{10m} > 6 \text{ m s}^{-1}$  just  
353 to the south of the cyclone center (Figure 1e). At 700 hPa wind speeds reach as high as  $18 \text{ m s}^{-1}$   
354 south of the cyclone center (Figure 1f).  
355

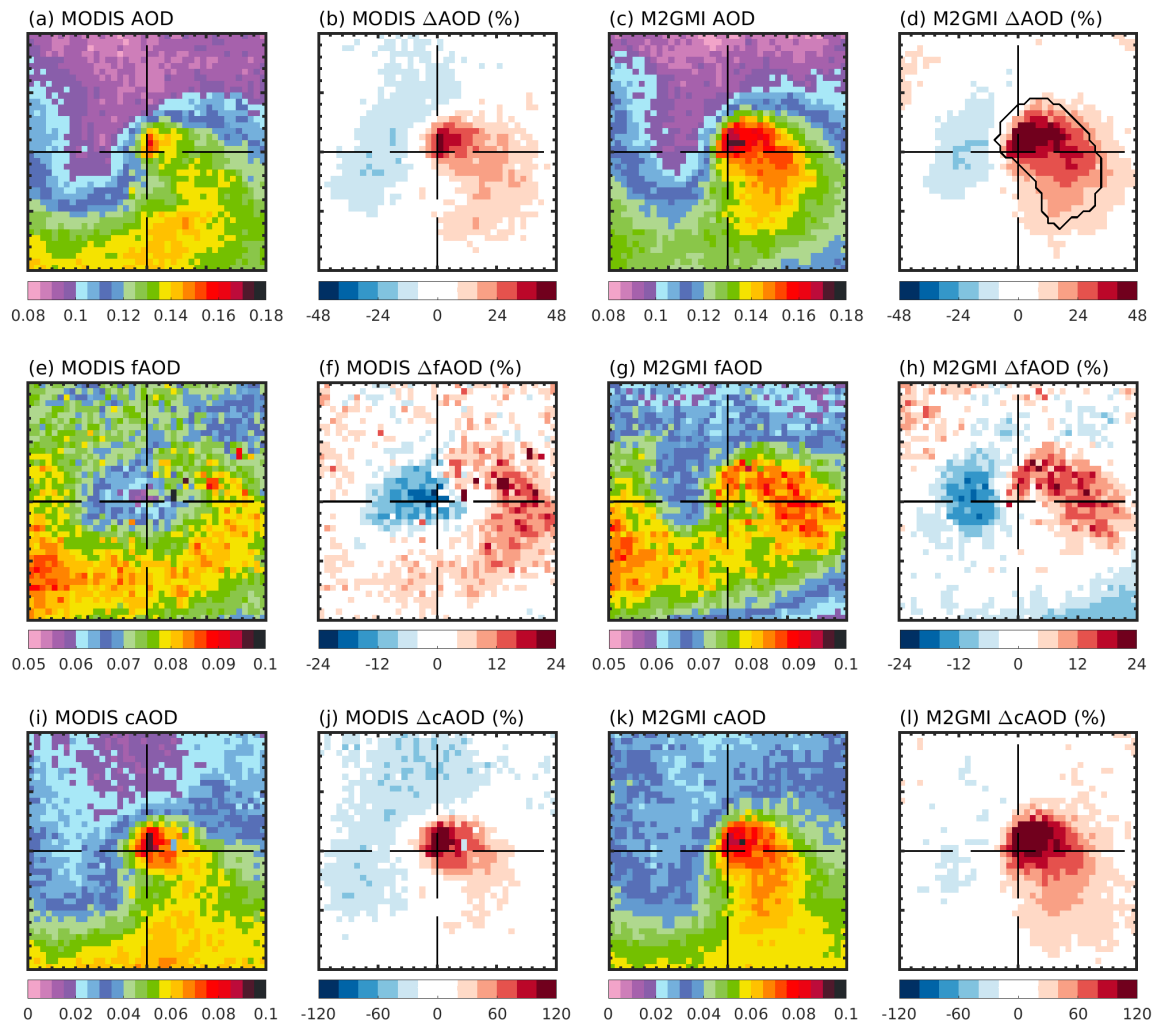
356 Figures 1g-i show the composites of 700 hPa AnthroCO<sub>25d</sub> from M2GMI. Both the  
357 cyclone and background composites display the largest concentrations of AnthroCO<sub>25d</sub> in the  
358 southwest of the domain, reflecting outflow from the polluted continental boundary layer. The  
359 cyclone composite also shows that as the WCB ascends and wraps into the cyclone center, it  
360 carries elevated AnthroCO<sub>25d</sub> (13-15 ppbv) offshore and into the free troposphere (Figure 1g).  
361 The  $\Delta$ AnthroCO<sub>25d</sub> composite highlights that cyclone WCBs enhance mean AnthroCO<sub>25d</sub> in the  
362 lower free troposphere by 15-30% compared to background conditions (Figure 1i). The  
363 composites also display a 5-10 % reduction in AnthroCO<sub>25d</sub> behind the cyclone as cleaner air is  
364 transported equatorward both from higher altitudes and latitudes in the DI.

## 365 4 Aerosol Optical Depth Composites

### 366 4.1 Annual Mean and Seasonal AOD Composites

367 Composites of MODIS Aqua AOD exhibit a pattern of elevated AOD to the east of the  
368 cyclone center in the WCB, with values of 0.13-0.16 (Figure 2a). Relative to background  
369 conditions, MODIS AOD is enhanced by 20-45% in the WCB, coinciding with the regions of  
370 enhanced vertical ascent, precipitation, and clouds (Figure 1). M2GMI predicts slightly higher  
371 AOD values (0.14-0.18) but captures the cyclone-wide features observed by MODIS quite well  
372 ( $r = 0.88$ ; Figure 2a-d), with enhancements of 30-50% above background. MODIS and M2GMI  
373 show similar decrease in AOD ( $\Delta$ AOD = -25%) to the west of the cyclone center in the DI  
374 (Figure 2a-d). These composites are based only on cloud-free grid cells within each cyclone, thus  
375 limiting the number of MODIS points available for the composites (Figure S2). Despite this,  
376 enough points remain to obtain coherent patterns of AOD.  
377

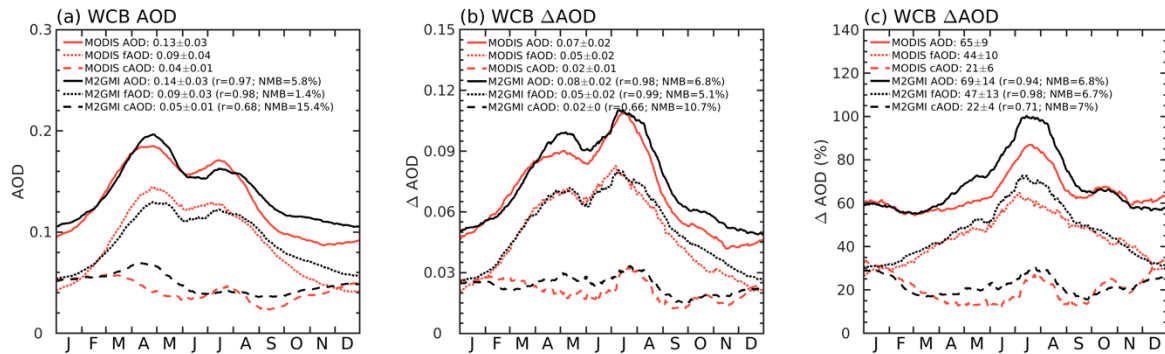
378 MODIS fAOD reaches values of 0.07-0.09 to the east and northeast of the cyclone center  
379 (Figure 3e). In this region M2GMI captures similar values of fAOD (0.07-0.1) but across a larger  
380 area that is spread out to the east (Figure 3g). For both MODIS and M2GMI, the fine mode  
381 fraction (FMF = fAOD / AOD) has values of 0.5-0.6 in the WCB. This is consistent with Naud et  
382 al. (2016) who found the breakdown of MODIS fine and coarse AOD to be about equal in the  
383 warm sector. Both MODIS and M2GMI show fAOD enhancements of 20-40% relative to  
384 background fAOD (Figures 3f,h). In addition, cAOD is maximum (>0.08) near the center of the  
385 composite, where it is enhanced by more than a factor of two relative to background cAOD  
386 (Figures 3i-l). We have applied this same procedure to the AOD from MODIS on the Terra  
387 satellite, finding similar results (Figure S3), with MODIS Terra AOD values being slightly larger  
388 than Aqua (e.g., Wei et al., 2019b).



389  
 390 **Figure 2.** Midlatitude cyclone composites of AOD, fine AOD (fAOD), coarse AOD (cAOD), and their  
 391 enhancements for MODIS Aqua (a, b, e, f, i, and j) and M2GMI (c, d, g, h, k, and l). Enhancements are expressed as  
 392 a percent relative to the respective backgrounds. The M2GMI AOD is sampled at the Aqua overpass time only when  
 393 there are valid MODIS AOD observations (section 3.2). The black contour in Figure 3d corresponds to the WCB  
 394 region as defined in section 4.1. The composites shown represent the same cyclones shown in Figure S1 and Figure  
 395 1.

396  
 397 For each cyclone, we identify the WCB as the outermost closed 700 hPa  $\omega$  contour  
 398 enclosing an  $\omega$  minimum (ascent maximum) within 1,000 km of the cyclone center. The black  
 399 contour in Figure 2d shows the area of the WCB when the identification procedure is carried out  
 400 on the  $\omega$  composite from Figure 1c. We calculate the mean AOD in the WCB region of each  
 401 cyclone and the resulting seasonal cycle in MODIS and M2GMI AOD is shown in Figure 3. The  
 402 WCB AOD observed by MODIS reaches its maximum in April and May, with a secondary  
 403 maximum in July. M2GMI reproduces the observed MODIS AOD well ( $r = 0.97$ ; NMB = 6%).  
 404 When expressed as a percent enhancement relative to background (Figure 3c) we find that  
 405 MODIS AOD is enhanced by 65% on average, with the highest enhancements occurring in July  
 406 (90%) when background AOD is at a minimum. Note that extracting AOD values within

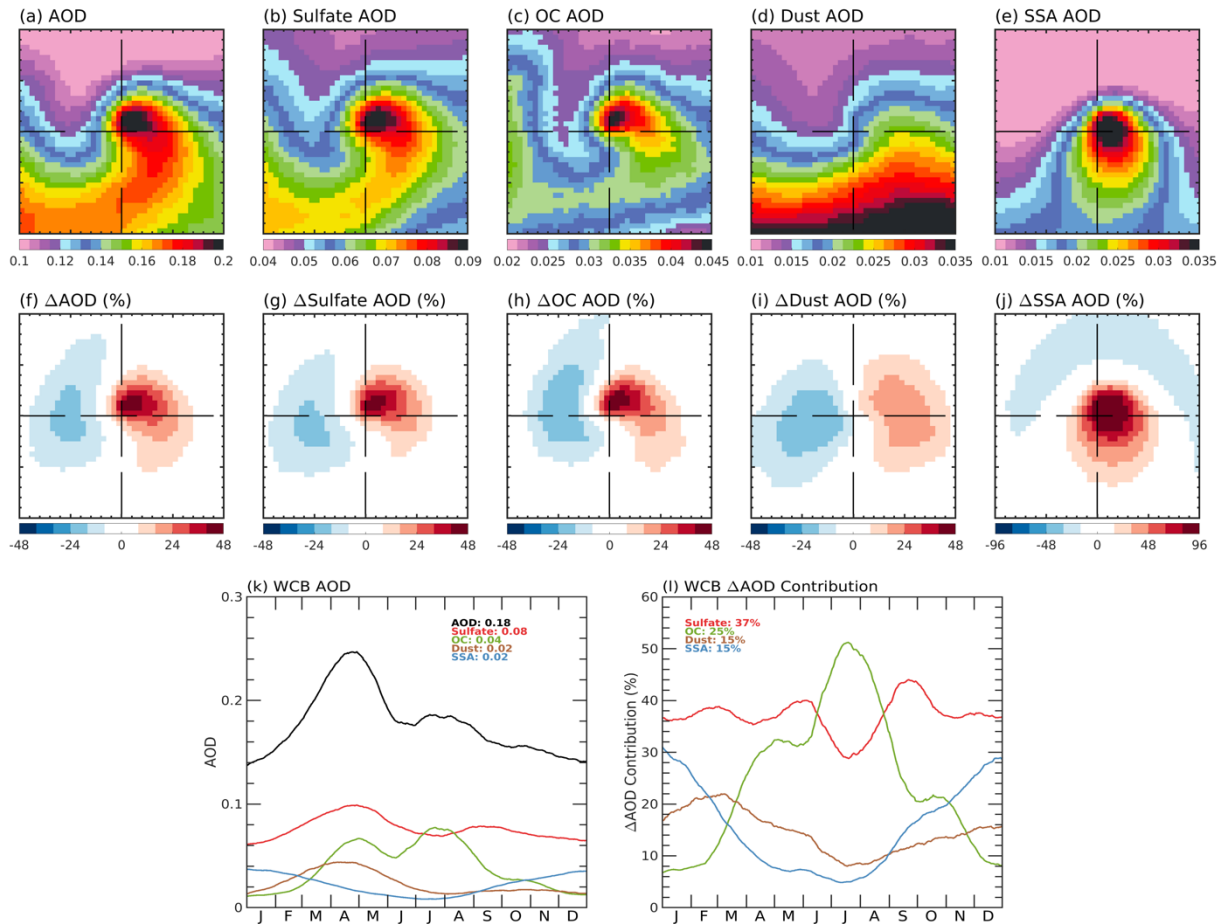
407 individual WCBs yields values larger than seen in the Figure 2 composites as application of the  
 408 identification criteria to each cyclone individually allows the location of the WCB to vary. We  
 409 find that fAOD accounts for 68% of the WCB  $\Delta$ AOD annually and has the same seasonal cycle  
 410 as  $\Delta$ AOD, maximizing in spring-summer (Figure 3). During December and January, when  
 411 cAOD reaches its maximum value, it accounts for half of AOD. We find similar results for  
 412 MODIS Terra (Figure S4). The M2GMI simulation captures the observed seasonality in WCB  
 413 AOD, the contributions from coarse and fine AOD, and their respective enhancements relative to  
 414 background (Figures 3 and S4).  
 415



416  
 417 **Figure 3.** (a) Composite seasonal cycle for AOD, fAOD, and cAOD in the warm conveyor belt of individual  
 418 cyclones (section 4.1). (b) Composite seasonal cycle for AOD, fAOD, and cAOD anomalies. (c) Same as (b) but  
 419 expressed a percent relative to the total AOD background. Values are shown for MODIS Aqua (orange lines) and  
 420 M2GMI (black lines). A 40-day boxcar smoothing has been applied to each time series. Annual mean values for  
 421 each timeseries are also given in the legend.

## 422 4.2 Contributions of Aerosol Species to AOD Composites

423 We now examine composites of the M2GMI simulation to understand the relative  
 424 contribution of individual aerosol species to the midlatitude cyclone AOD composites (Figure 4).  
 425 Here, we use daily mean M2GMI values instead of the 2pm Aqua overpass time. Furthermore,  
 426 we do not apply any sampling relative to MODIS data availability or CF such that the  
 427 composites include both cloudy and cloud-free regions of the midlatitude cyclones. Figure 4a  
 428 shows that the WCB stands out as a region of large AOD ( $>0.2$ ) to the east of the cyclone center,  
 429 with values that are 25-30% larger than those in Figure 2c due the inclusion of cloudy regions.



430  
 431 **Figure 4.** Top row: midlatitude cyclone composites of M2GMI AOD for (a) total, (b) sulfate, (c) organic carbon, (d)  
 432 dust, (e) SSA. Middle row: Same as top row but expressed as anomalies relative to background values. For  
 433 individual aerosol species, the background is defined relative to that species (i.e.,  $\Delta AOD_{\text{dust}} = 100 \times (AOD_{\text{dust}} -$   
 434  $AOD_{\text{dust, background}}) / AOD_{\text{dust, background}}$ ). Bottom row: seasonal cycle of WCB M2GMI AOD (k) and contributions of  
 435 individual aerosol species to  $\Delta AOD$  (l). The timeseries have been smoothed with a 40-day boxcar average and  
 436 annual mean values for each species are given in the legend. Black carbon and nitrate aerosol (not shown)  
 437 contribute less than 10% of the  $\Delta AOD$ .  
 438

439 The cyclone composites of sulfate and OC display similar shapes (Figures 4b,g and 4c,h),  
 440 reflecting vertical transport of these aerosols and/or their precursors in the WCB. Dust  
 441 enhancements maximize at 30% in a region extending to the east of the cyclone center (Figure  
 442 4d,i), while SSA is strongly enhanced near the cyclone center (Figure 4e,j). Figure 4l shows  
 443 sulfate accounts for 37% of the  $\Delta AOD$ , followed by OC (25%), dust (15%), and SSA (15%).  
 444

445 Figure 4k helps interpret the seasonality of WCB AOD observed by MODIS: the spring  
 446 maximum is driven by sulfate, with smaller contributions from OC and dust, while the summer  
 447 secondary maximum follows the seasonality of OC, with smaller contributions from sulfate. In  
 448 M2GMI the summer maximum in OC is due to a combination of high emissions of OC from  
 449 fires and of biogenic volatile organic compounds. SSA AOD maximizes in winter and reaches its  
 450 lowest values in summer, following the seasonality of  $u_{10m}$  in midlatitude cyclones (Field &  
 451 Wood, 2007).

452

### 4.3 Variability of AOD Enhancements in Cyclone WCBs

453

454

455

456

457

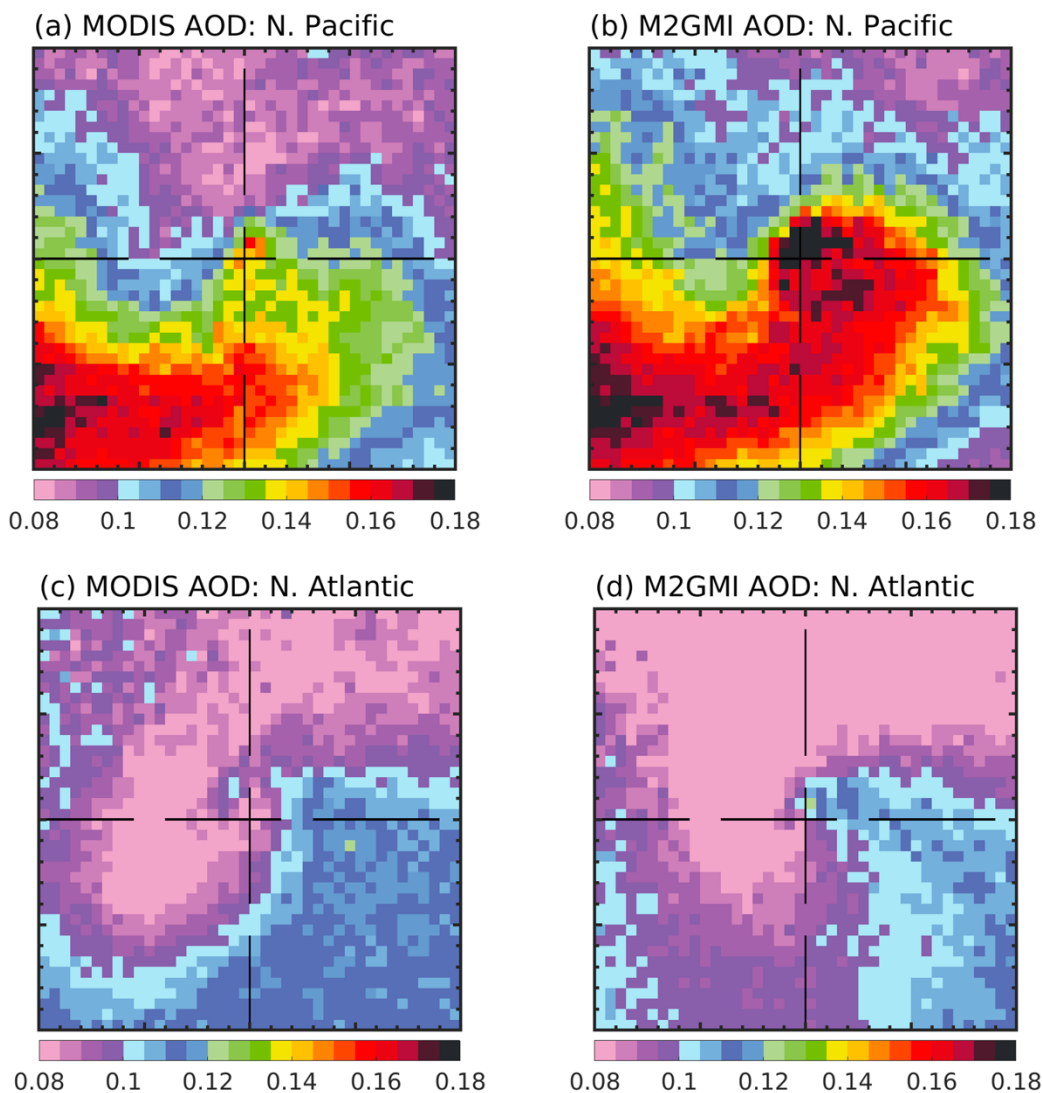
458

459

460

461

We now examine variability in total AOD by storm track region, analyzing 11,140 midlatitude cyclones with centers in the N. Pacific (30-80° N, 110°E – 120°W) and 8,724 cyclones in the N. Atlantic (30-80°N, -90°E – 20°E). We find that N. Pacific midlatitude cyclones have AODs that are 60% larger compared to N. Atlantic cyclones (Figure 5), consistent with larger emissions of pollution from Asia relative to North America. This inter-basin difference is seen in both the MODIS and M2GMI composites with M2GMI overestimating AOD in N. Pacific cyclones by 11%. M2GMI underestimates AOD in N. Atlantic cyclones by 8%.



462

463

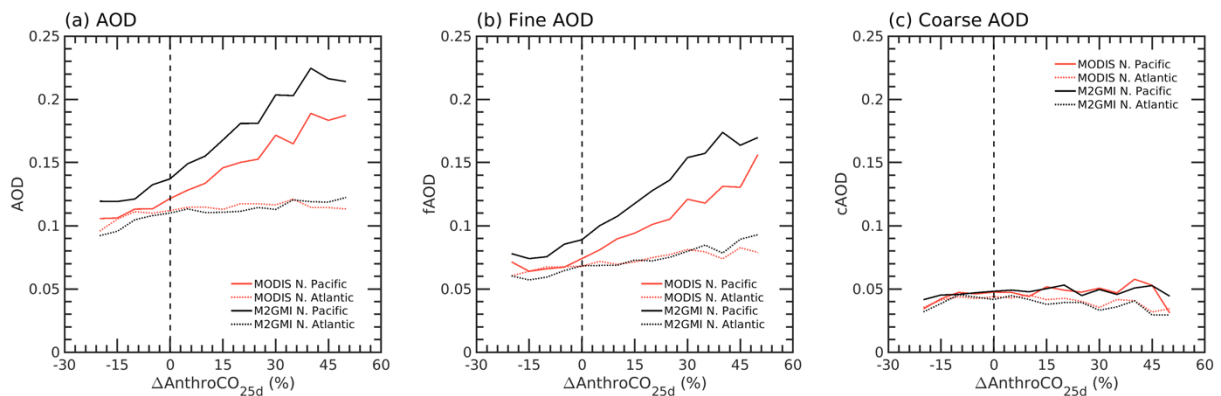
464

465

466

**Figure 5.** Midlatitude cyclone AOD  $\Delta$ AOD in the (a,b) N. Pacific (11,140 cyclones) and (c,d) N. Atlantic (8,724 cyclones) for MODIS (left) and M2GMI (right). M2GMI AOD is sampled at the Aqua overpass time only when there are valid MODIS AOD observations and CF <50% (section 3.2).

467 To further characterize storm track variability in the WCB of midlatitude cyclones, we  
 468 examine how AOD varies with 700 hPa  $\Delta\text{AnthroCO}_{25d}$ , which we use as a proxy for pollution.  
 469 We grouped cyclone WCBs in 5%  $\Delta\text{AnthroCO}_{25d}$  bins. In the N. Pacific storm track MODIS  
 470 AOD increases with increasing WCB pollution levels, nearly doubling from 0.11 to 0.19 (Figure  
 471 6a). This relationship is much weaker for N. Atlantic WCBs, with AOD increasing from 0.09 to  
 472 0.11. Most of the increase in AOD with increasing pollution is due to increases in fAOD (Figure  
 473 6b), while cAOD remains nearly invariant (Figure 6c). In WCBs with negative  $\Delta\text{AnthroCO}_{25d}$ ,  
 474 which correspond to midlatitude cyclones drawing air from the clean marine boundary layer,  
 475 fAOD constitutes just over half of the AOD whereas for cyclones with large  $\Delta\text{AnthroCO}_{25d}$  it  
 476 constitutes nearly 80%. M2GMI captures the observed relationships reasonably well, but  
 477 overestimates N. Pacific AOD and fAOD by 6-20% (Figure 6).  
 478



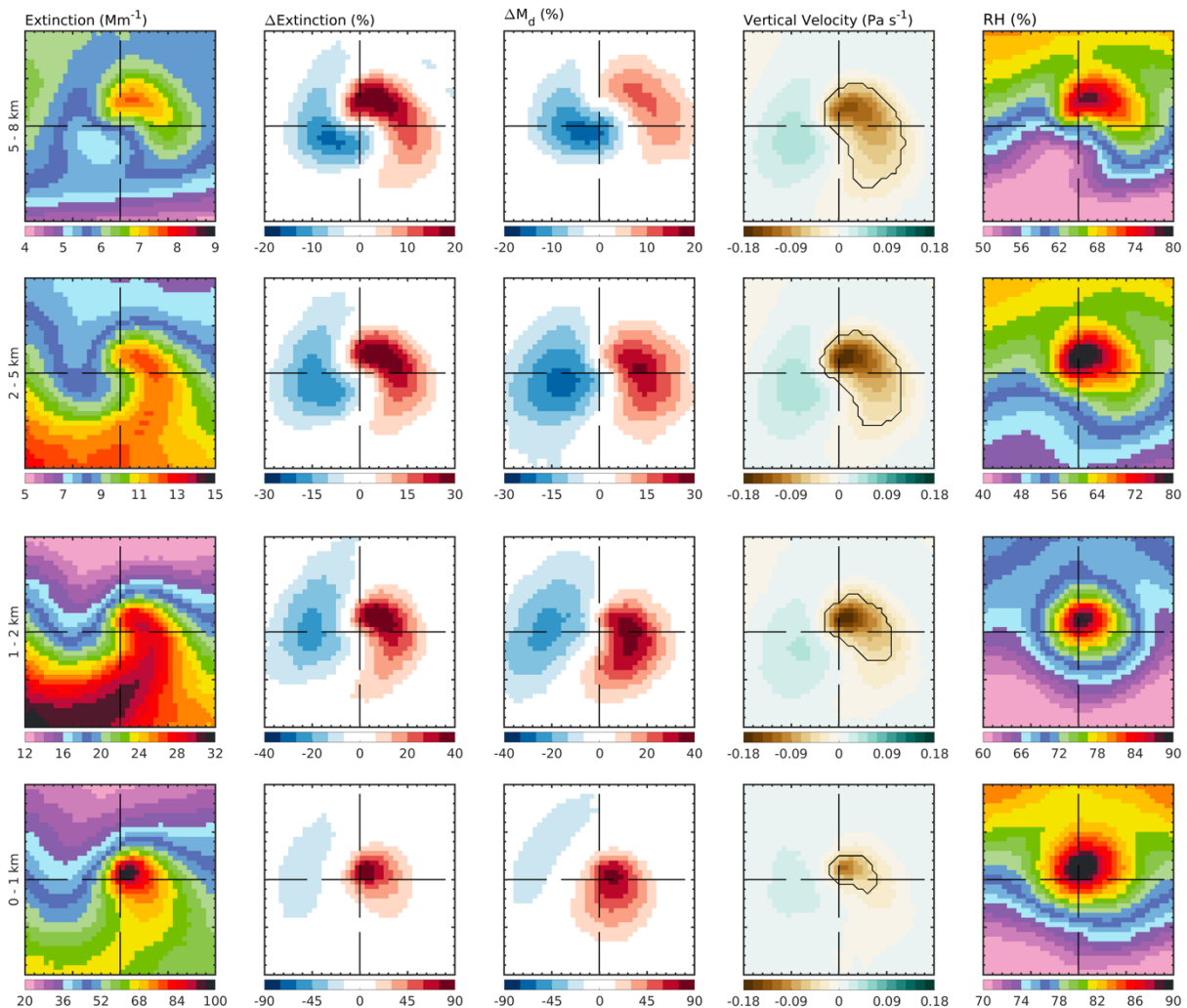
479  
 480 **Figure 6.** Relationship between AOD and anthropogenic pollution ( $\Delta\text{AnthroCO}_{25d}$ ) in the WCB of individual  
 481 cyclones: (a) total AOD, (b) fAOD, and (c) cAOD. Cyclones have been grouped in 5% bins based on M2GMI  
 482  $\Delta\text{AnthroCO}_{25d}$ . Values for MODIS (orange lines) and M2GMI (black lines) are separated between the N. Pacific  
 483 (solid lines) and N. Atlantic (dashed lines) basins.  
 484

485 The dependence of individual aerosol species in M2GMI with  $\Delta\text{AnthroCO}_{25d}$  (Figure S5)  
 486 shows that sulfate explains most of the AOD and fAOD differences between the N. Pacific and  
 487 N. Atlantic storm tracks. In N. Pacific midlatitude cyclones, M2GMI shows that sulfate, OC, and  
 488 dust all increase with  $\Delta\text{AnthroCO}_{25d}$  – reflecting their continental origin. Sulfate accounts for  
 489 65% of the strong increase in AOD with increasing pollution in the N. Pacific with OC and dust  
 490 accounting for 14% and 7%, respectively. SSA displays behavior opposite to that of the  
 491 continental aerosols, with a small decrease in AOD as  $\Delta\text{AnthroCO}_{25d}$  increases. Together, the  
 492 opposite behavior of dust and SSA with pollution help explain the near invariance of cAOD with  
 493 increasing  $\Delta\text{AnthroCO}_{25d}$  (Figure 6c).

## 494 5 Vertical Distribution of Aerosol Extinction and Mass

495 Figure 7 shows composites of M2GMI total aerosol extinction, aerosol extinction  
 496 enhancement, aerosol dry mass enhancement ( $\Delta M_d$ ),  $\omega$ , and RH between the surface and 8 km  
 497 altitude. To calculate the overall  $\Delta M_d$ , the individual component dry mass enhancements have  
 498 been weighted by their contribution to the background AOD in M2GMI. Aerosol extinction is  
 499 enhanced by more than 20-40% through a deep layer extending from the surface to 8 km in the  
 500 WCB (Figure 7). This enhancement in extinction coincides with strong upward motion and high  
 501 RH at all levels. As the WCB ascends above 1-2 km, it begins to spread out to the east and

502 northeast, wrapping cyclonically with the DI, which transports cleaner air (Figure 7). This is  
 503 indicative of our selection of midlatitude cyclones being dominated by stronger, cut-off cyclones  
 504 (Whitaker et al., 1988).  
 505



506 **Figure 7.** Composites of M2GMI layer mean total aerosol extinction (first column;  $\text{Mm}^{-1}$ ),  $\Delta$  extinction (second  
 507 column; %), aerosol dry mass enhancement ( $\Delta M_a$ , third column; %), vertical velocity ( $\omega$ , fourth column;  $\text{Pa s}^{-1}$ ), and  
 508 RH (fifth column, %) for 2005-2018 NH midlatitude cyclones. The  $\Delta M_a$  has been weighted according to each  
 509 aerosol component's contribution to the background extinction (section 5). The altitude layers correspond to 5-8 km  
 510 (top row), 2-5 km (second row), 1-2 km (third row), and 0-1 km (bottom row). The black contours in the third  
 511 column represent the average extent of the warm conveyor belt airstream (as defined in section 4.1 of the text).  
 512  
 513

514 Vertical profiles of M2GMI extinction in the WCB show that below 1km in altitude, the  
 515 extinction is dominated by sulfate and SSA, which together account for  $\sim 75\%$  of the  
 516 enhancement in total extinction (Figure S6). SSA extinction rapidly declines away from the  
 517 surface, but sulfate is the largest contributor to extinction throughout much of the profile,  
 518 followed by OC and dust. The contribution of dust to the total extinction enhancement reaches  
 519 20% between 2.5-5.5 km. These results are consistent with Luan & Jaeglé (2013), who found  
 520 sulfate export to occur at altitudes between 1-3 km and 2-6 km off North America and Asia,  
 521 respectively. They are also consistent with He et al. (2012) who noted elevated concentrations of

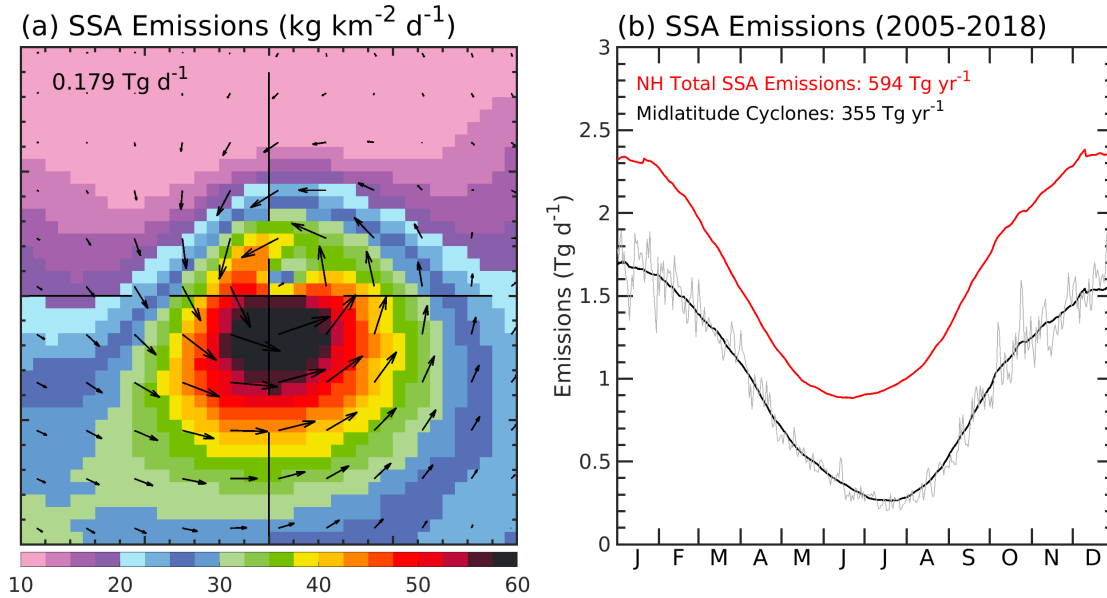
522 sulfate precursors in the free troposphere between 2-4 km over China in spring. While dust  
523 aerosols may be lifted in the WCB, much of the signature in the profiles likely comes from  
524 horizontal export of dust from high altitude desert regions in Asia (e.g., Eguchi et al., 2009;  
525 Huang et al., 2008).

526  
527 How much of the enhanced AOD in the WCB is due to humidification as opposed to  
528 increased aerosol mass? To first order,  $\Delta\text{Extinction}$  is equal to the sum of  $\Delta M_d$  and the  
529 enhancement in aerosol mass extinction efficiency ( $\Delta\beta$ ), which includes humidification effects  
530 (SI Text 1). Near the surface,  $\Delta\text{Extinction}$  and  $\Delta M_d$  display similar values, reaching 90% (Figure  
531 7), which implies only a small contribution of humidification effects in the already very humid  
532 boundary layer. As the WCB ascends, the two enhancements begin to diverge, with  $\Delta M_d$   
533 decreasing more rapidly than  $\Delta\text{Extinction}$ , indicative of an increasing contribution of  
534 humidification effects on extinction. For example, in the 5-8km layer  $\Delta\text{Extinction}$  maximizes at  
535 20% while  $\Delta M_d$  reaches only 10-12% (Figure 7). Overall, we find that aerosol growth by  
536 humidification accounts for ~40% of the  $\Delta\text{AOD}$  in cyclone WCBs (Figure S7).

## 537 **6 Midlatitude Cyclone Sea Salt Aerosol Emissions and Net Effect on NH Aerosols**

### 538 **6.1 Midlatitude Cyclones as a Source of SSA**

539 We now quantify the contribution of midlatitude cyclones as a source of SSA. Figure 8a  
540 shows the M2GMI mean composite of SSA emissions for all NH midlatitude cyclones in 2005-  
541 2018. A core of large emissions ( $>40 \text{ kg km}^{-2} \text{ d}^{-1}$ ) occurs 100-500 km south of the cyclone  
542 center. We calculate total SSA emissions in the high wind speed region ( $u_{10m} > 5 \text{ m s}^{-1}$ ) within  
543 2,000 km of the cyclone center for the composite and find that, on average, a NH midlatitude  
544 cyclone leads to SSA emissions of  $0.179 \text{ Tg d}^{-1}$ . We apply the same approach to calculate SSA  
545 emissions for each individual midlatitude cyclone and show the resulting seasonal cycle in  
546 Figure 8b. Annually, high winds associated with midlatitude cyclones emit  $355 \text{ Tg yr}^{-1}$ ,  
547 compared to the total SSA emissions of  $594 \text{ Tg yr}^{-1}$  in the 30-80°N region. Thus, midlatitude  
548 cyclones account for 60% of the total SSA emissions. The region of high cyclone winds over  
549 which we integrate SSA emissions covers 40% of the NH ocean area annually (Figure S8).  
550 Therefore, midlatitude cyclones account for more than twice as much SSA emissions per surface  
551 area as the rest of the NH oceans. SSA emissions from midlatitude cyclones maximize in winter  
552 ( $1.5\text{-}1.8 \text{ Tg d}^{-1}$ ) and decrease to a summer minimum of  $0.3\text{-}0.5 \text{ Tg d}^{-1}$ . This seasonal variability  
553 follows from the seasonal variability in  $u_{10m}$  (Figure S8).

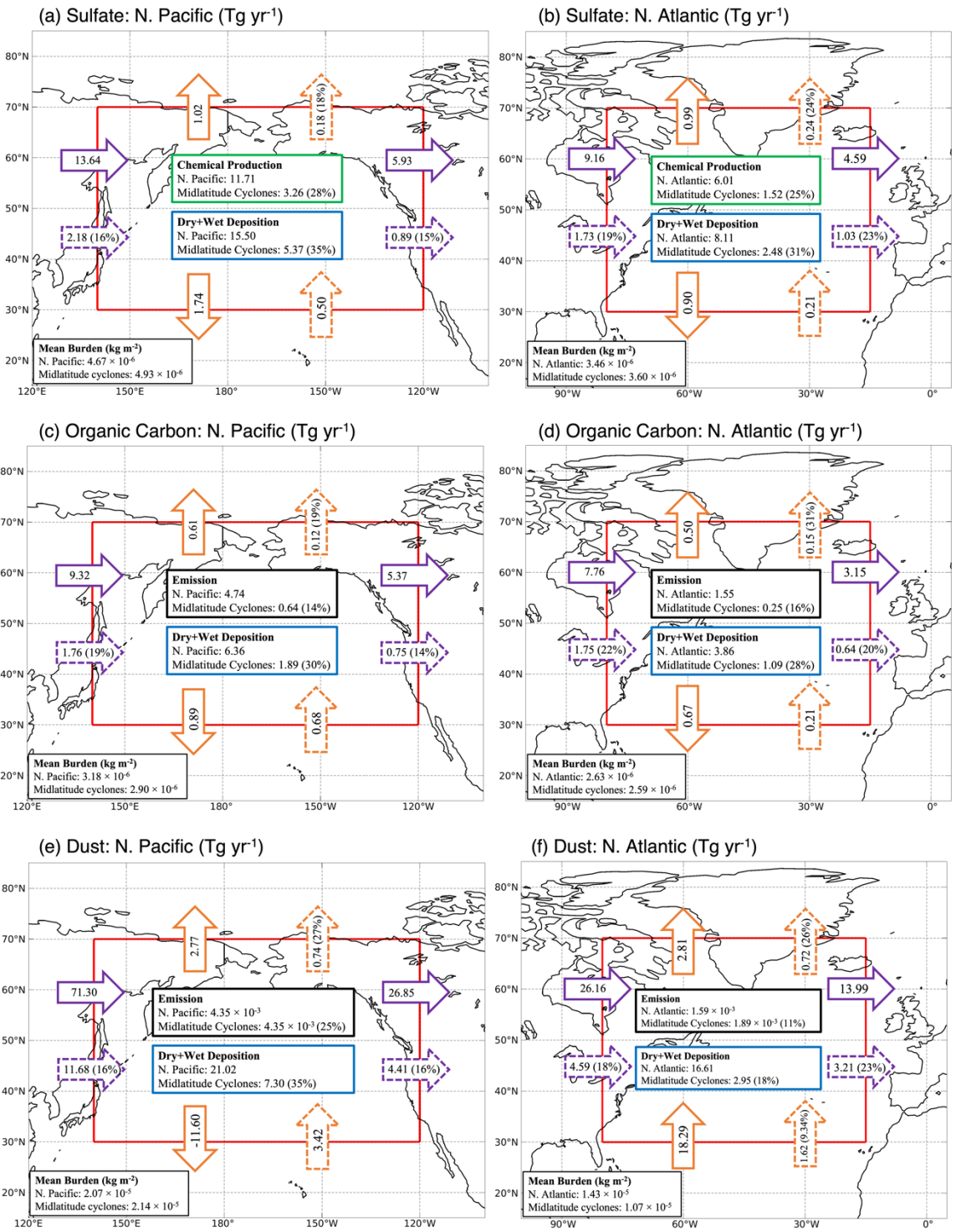


554  
 555 **Figure 8.** (a) Cyclone composite of SSA emissions (kg km<sup>-2</sup> d<sup>-1</sup>). The mean daily composite SSA emissions  
 556 calculated as in section 6.1 is given in the top left of the panel. Composite u<sub>10m</sub> vector winds are represented by  
 557 arrows. (b) Annual cycle of NH midlatitude cyclone SSA emissions calculated over the high wind-speed region for  
 558 each cyclone (u<sub>10m</sub> > 5 m s<sup>-1</sup>, 30-80°N). Daily emissions are in gray while the black line shows emissions smoothed  
 559 with a 40-day boxcar average). The multiyear mean SSA emissions for 30-80°N emissions is shown in red.

## 560 6.2 Net effect of Midlatitude Cyclones on NH Aerosol Budgets

561 We use the M2GMI simulation to isolate the contribution of midlatitude cyclone WCBs  
 562 to the budgets of sulfate, OC, and dust over the NH midlatitude oceans, separating the N. Pacific  
 563 (30 – 70°N, 140°E – 120°W) and N. Atlantic (30 – 70°N, 80°W – 15°W) basins. For each day and  
 564 basin, we extract the basin-wide burden, chemical production (for sulfate), dry+wet deposition,  
 565 emission, and horizontal fluxes. We do the same for individual midlatitude cyclones, using  
 566 WCBs defined by 700 hPa ω (section 4.1). We also average over the 2005-2018 period to  
 567 construct a mean annual cycle for both the entire basin and cyclones.

568 Figure 9 summarizes the 2005-2018 annual mean budgets for sulfate, OC, and dust.  
 569 Basin-wide fluxes are represented by solid arrows while midlatitude cyclone WCBs are denoted  
 570 by dashed arrows. Comparing the basin-wide and cyclone values in the N. Pacific, we find that  
 571 midlatitude cyclone WCBs contribute 16-20% of the sulfate, OC, and dust horizontal fluxes  
 572 along 140°E. The contribution of WCB to fluxes into the N. Pacific maximize in spring at 30%.  
 573 The seasonality and contribution of WCBs to fluxes along 80°W in the N. Atlantic is similar (18-  
 574 22%). On the eastern edge of the basins, cyclone WCBs contribute 14-23% of fluxes out of the  
 575 NH basins (maximizing at 20-30% in spring). In addition, midlatitude cyclones account for a  
 576 significant fraction of the aerosol flux to polar regions, with contributions ranging from 18-24%  
 577 for sulfate, 19-31% for OC, and 26-27% for dust.



578  
579  
580  
581  
582  
583

**Figure 9.** Annual mean 2005-2018 aerosol budgets within northern hemisphere ocean basins (units Tg yr<sup>-1</sup>). (a,c,e) N. Pacific basin (30 – 70°N, 140°E – 120°W, red outline). (b,d,f) N. Atlantic basin (30 – 70°N, 80°W – 15°W, red outline). In each panel solid arrows represent horizontal advective fluxes through the boundaries, while dashed arrows represent fluxes associated with midlatitude cyclone WCBs. The annual mean basin-wide and midlatitude cyclone burden (units kg m<sup>-2</sup>) are given in the bottom left of each panel.

584 Large-scale precipitation associated with WCBs results in efficient dry+wet deposition of  
585 aerosols, accounting for ~30% of the sulfate, OC, and dust deposition over the N. Pacific and N.  
586 Atlantic basins. This contribution varies seasonally, ranging from 50% in spring to 20% in  
587 summer. In the N. Pacific, WCBs cover 18% of the area annually while in the N. Atlantic they  
588 cover 15% of the area annually. Therefore, midlatitude cyclone WCBs are about twice as  
589 efficient at scavenging aerosols as the broader NH basins.

590  
591 Annually in the N. Pacific, we find WCBs lead to 3.26 Tg yr<sup>-1</sup> of sulfate production, 80%  
592 of which occurs through aqueous SO<sub>2</sub> oxidation in the extensive cyclone cloud cover. Basin-  
593 wide production of sulfate aerosol is 11.71 Tg yr<sup>-1</sup> in the N. Pacific, meaning WCBs contribute  
594 28% to the total. WCB contributions range from 10% (summer) to 40% (spring). Comparing  
595 these values to the deposition and fluxes of sulfate is consistent with its evolution following the  
596 conceptual models put forth in Brock et al. (2004) and Dunlea et al. (2009). Cyclone WCBs  
597 efficiently scavenge sulfate aerosol such that the increases in WCB sulfate mass relative to the  
598 basin-wide average are due to export of SO<sub>2</sub> followed by its oxidation in midlatitude cyclones.  
599 WCBs contribute similarly to sulfate production in the N. Atlantic (1.52 Tg yr<sup>-1</sup> resulting in a  
600 25% contribution).

## 601 **7 Conclusions**

602 Our analysis systematically examined AOD and aerosol distributions in midlatitude  
603 cyclones and linked processes in the WCB and broader cyclone environment to aerosol  
604 emissions and export to the global atmosphere. The composites of 27,707 NH midlatitude  
605 cyclones over a 14-year period show a 25-45% increase in AOD observed by MODIS to the east  
606 of the cyclone center. These enhancements are co-located with heavy precipitation, extensive  
607 cloud cover, vertical motions, and high RH in the cyclone WCB. The M2GMI simulation shows  
608 a 30-50% increase in AOD in the same region. AOD and ΔAOD in cyclone WCBs maximize in  
609 spring due to a large contribution (>70% of the total) from fine mode aerosols. Annually, fine  
610 aerosols accounts for 70% of the ΔAOD in MODIS and 63% in M2GMI. Overall, we find the  
611 M2GMI simulation captures the magnitude and seasonality of the MODIS observations.

612  
613 M2GMI composites of individual aerosol species AOD show that cyclones enhance AOD  
614 by up to 40% for sulfate, 50% for OC, 25% for dust, and 130% for SSA. The contribution of  
615 sulfate to the total ΔAOD is consistent throughout the year at 30-40%. The contribution of the  
616 other components shows large variability. The contribution of SSA ranges from 30% in fall-  
617 winter to <10% in summer while the contribution of OC ranges from <10% in winter to >50% in  
618 July and August. The contribution of dust maximizes at 20% in spring. Larger pollutant  
619 emissions in Asia lead to 60% larger AODs in N. Pacific WCBs than those in the N. Atlantic.  
620 This also leads to a stronger relationship between WCB pollution and sulfate and OC AODs in  
621 N. Pacific WCBs.

622  
623 We find that the high surface winds associated with midlatitude cyclones account for 355  
624 Tg yr<sup>-1</sup> of SSA emissions annually, which constitutes 60% of the 30–80° N SSA emissions. Our  
625 compositing approach also highlights the net effect of midlatitude cyclones on aerosol budgets  
626 over the NH oceans. WCBs facilitate export of aerosols to and from the N. Pacific and N.  
627 Atlantic basins, accounting for ~16-22% of the horizontal advective fluxes on the western and  
628 eastern boundaries, and ~18-31% of transport to polar regions. We find that largescale

629 precipitation in cyclone WCBs efficiently removes aerosols such that they contribute 27-33% to  
630 deposition over the N. Pacific and N. Atlantic basins while only covering 15-18% of the area. In  
631 addition, WCB export of SO<sub>2</sub> followed by its in-cloud oxidation accounts for 25-28% of the total  
632 chemical production of sulfate in the N. Pacific and N. Atlantic basins.

633  
634 Aerosols remain a highly uncertain part of the climate future (Szopa et al., 2021)  
635 particularly due to changing anthropogenic emissions. As societies transition away from energy  
636 sources that emit greenhouse gases, it is likely that anthropogenic aerosol emissions will also  
637 decrease (Larson & Portmann, 2019). Nevertheless, results from the Coupled Model  
638 Intercomparison Project Phase 6 suggest increases in urban particulate matter even in scenarios  
639 with some climate mitigation actions (Turnock et al., 2020). In addition, transport pathways may  
640 change in the future as the spatiotemporal variability of midlatitude cyclones changes. While  
641 disagreement exists in projections of the NH storm tracks, one consistent projection is a  
642 seasonally non-uniform poleward shift (Simpson et al., 2014) coupled with an overall reduction  
643 in frequency (Chang et al., 2012). Recent projections also suggest an increase in midlatitude  
644 cyclone precipitation under future climate scenarios (Catto et al., 2019) that could act to increase  
645 aerosol removal during transport. Taken together, these projections may suggest an overall  
646 reduction in aerosol export to the global atmosphere by cyclone WCBs with a simultaneous  
647 increase in aerosol abundances for the most polluted cyclones.

## 648 **Acknowledgements**

649 This work was supported under NSF award number 1901786. MERRA-2 GMI is supported by  
650 the NASA Modeling, Analysis, and Prediction (MAP) program and the high-performance  
651 computing resources were provided by the NASA Center for Climate Simulation (NCCS).

## 652 **Open Research**

653 MODIS collection 6.1 observations used in this study are available for download at the  
654 following: <https://ladsweb.modaps.eosdis.nasa.gov/archive/allData/61/>. The MERRA-2 GMI  
655 data used in this study are a product of the NASA GMAO and are available at the following:  
656 [https://portal.nccs.nasa.gov/datashare/merra2\\_gmi/](https://portal.nccs.nasa.gov/datashare/merra2_gmi/). The cyclone-centered grids used in the  
657 compositing are available in netCDF format upon request.

## 658 **8 References**

- 659 Alfaro, C., & Gomes, L. (2001). Modeling mineral aerosol production by wind erosion : Emission Particles enough.  
660 *Geophysical Research*, 106(D16), 75–84.
- 661 Andreae, M. O., & Crutzen, P. J. (1997). Atmospheric aerosols: Biogeochemical sources and role in atmospheric  
662 chemistry. *Science*, 276(5315), 1052–1058. <https://doi.org/10.1126/science.276.5315.1052>
- 663 Baker, A. R., Kelly, S. D., Biswas, K. F., Witt, M., & Jickells, T. D. (2003). Atmospheric deposition of nutrients to  
664 the Atlantic Ocean. *Geophysical Research Letters*, 30(24), 2–5. <https://doi.org/10.1029/2003GL018518>
- 665 Bian, H., Chin, M., Hauglustaine, D. A., Schulz, M., Myhre, G., Bauer, S. E., ... Tsyro, S. G. (2017). Investigation  
666 of global particulate nitrate from the AeroCom phase III experiment. *Atmospheric Chemistry and Physics*,  
667 17(21), 12911–12940. <https://doi.org/10.5194/acp-17-12911-2017>
- 668 Bian, H., Froyd, K., Murphy, D. M., Dibb, J., Darmenov, A., Chin, M., ... Smirnov, A. (2019). Observationally  
669 constrained analysis of sea salt aerosol in the marine atmosphere. *Atmospheric Chemistry and Physics*, 19(16),  
670 10773–10785. <https://doi.org/10.5194/acp-19-10773-2019>
- 671 Booth, J. F., Naud, C. M., & Jeyaratnam, J. (2018). Extratropical Cyclone Precipitation Life Cycles: A Satellite-  
672 Based Analysis. *Geophysical Research Letters*, 45(16), 8647–8654. <https://doi.org/10.1029/2018GL078977>

673 Brock, C. A., Hudson, P. K., Lovejoy, E. R., Sullivan, A., Nowak, J. B., Huey, L. G., ... Wilson, J. C. (2004).  
674 Particle characteristics following cloud-modified transport from Asia to North America. *Journal of*  
675 *Geophysical Research D: Atmospheres*, 109(23), 1–17. <https://doi.org/10.1029/2003JD004198>  
676 Browning, K. A. (1997). The dry intrusion perspective of extra-tropical cyclone development. *Meteorological*  
677 *Applications*, 4(4), S1350482797000613. <https://doi.org/10.1017/S1350482797000613>  
678 Browning, K. A., & Roberts, N. M. (1994). Structure of a frontal cyclone. *Quarterly Journal of the Royal*  
679 *Meteorological Society*, 120(520), 1535–1557. <https://doi.org/10.1002/qj.49712052006>  
680 Catto, J. L., Ackerley, D., Booth, J. F., Champion, A. J., Colle, B. A., Pfahl, S., ... Seiler, C. (2019). The Future of  
681 Midlatitude Cyclones. *Current Climate Change Reports*, 5(4), 407–420. [https://doi.org/10.1007/s40641-019-](https://doi.org/10.1007/s40641-019-00149-4)  
682 00149-4  
683 Catto, J. L., Shaffrey, L. C., & Hodges, K. I. (2010). Can climate models capture the structure of extratropical  
684 cyclones? *Journal of Climate*, 23(7), 1621–1635. <https://doi.org/10.1175/2009JCLI3318.1>  
685 Chang, E. K. M., Guo, Y., & Xia, X. (2012). CMIP5 multimodel ensemble projection of storm track change under  
686 global warming. *Journal of Geophysical Research Atmospheres*, 117(23), 1–19.  
687 <https://doi.org/10.1029/2012JD018578>  
688 Chin, M., Diehl, T., Tan, Q., Prospero, J. M., Kahn, R. A., Remer, L. A., ... Torres, O. (2014). Multi-decadal  
689 aerosol variations from 1980 to 2009: A perspective from observations and a global model. *Atmospheric*  
690 *Chemistry and Physics*, 14(7), 3657–3690. <https://doi.org/10.5194/acp-14-3657-2014>  
691 Chin, Mian, Diehl, T., Dubovik, O., Eck, T. F., Holben, B. N., Sinyuk, A., & Streets, D. G. (2009). Light absorption  
692 by pollution, dust, and biomass burning aerosols: A global model study and evaluation with AERONET  
693 measurements. *Annales Geophysicae*, 27(9), 3439–3464. <https://doi.org/10.5194/angeo-27-3439-2009>  
694 Chin, Mian, Ginoux, P., Kinne, S., Torres, O., Holben, B. N., Duncan, B. N., ... Nakajima, T. (2002). Tropospheric  
695 aerosol optical thickness from the GOCART model and comparisons with satellite and sun photometer  
696 measurements. *Journal of the Atmospheric Sciences*, 59(3 PT 1), 461–483. [https://doi.org/10.1175/1520-](https://doi.org/10.1175/1520-0469(2002)059<0461:taotft>2.0.co;2)  
697 0469(2002)059<0461:taotft>2.0.co;2  
698 Colarco, P., Da Silva, A., Chin, M., & Diehl, T. (2010). Online simulations of global aerosol distributions in the  
699 NASA GEOS-4 model and comparisons to satellite and ground-based aerosol optical depth. *Journal of*  
700 *Geophysical Research Atmospheres*, 115(14). <https://doi.org/10.1029/2009JD012820>  
701 Ding, A., Wang, T., Xue, L., Gao, J., Stohl, A., Lei, H., ... Zhang, X. (2009). Transport of north China air pollution  
702 by midlatitude cyclones: Case study of aircraft measurements in summer 2007. *Journal of Geophysical*  
703 *Research Atmospheres*, 114(8), 1–16. <https://doi.org/10.1029/2008JD011023>  
704 Duncan, B. N., Strahan, S. E., Yoshida, Y., Steenrod, S. D., & Livesey, N. (2007). Model study of the cross-  
705 tropopause transport of biomass burning pollution. *Atmospheric Chemistry and Physics*, 7(14), 3713–3736.  
706 <https://doi.org/10.5194/acp-7-3713-2007>  
707 Dunlea, E. J., Decarlo, P. F., Aiken, A. C., Kimmel, J. R., Peltier, R. E., Weber, R. J., ... Jimenez, J. L. (2009).  
708 Evolution of Asian aerosols during transpacific transport in INTEX-B. *Atmospheric Chemistry and Physics*,  
709 9(19), 7257–7287. <https://doi.org/10.5194/acp-9-7257-2009>  
710 Eckhardt, S., Stohl, A., Wernli, H., James, P., Forster, C., & Spichtinger, N. (2004). A 15-year climatology of warm  
711 conveyor belts. *Journal of Climate*, 17(1), 218–237. [https://doi.org/10.1175/1520-](https://doi.org/10.1175/1520-0442(2004)017<0218:AYCOWC>2.0.CO;2)  
712 0442(2004)017<0218:AYCOWC>2.0.CO;2  
713 Eguchi, K., Uno, I., Yumimoto, K., Takemura, T., Shimizu, A., Sugimoto, N., & Liu, Z. (2009). Trans-pacific dust  
714 transport: Integrated analysis of NASA/CALIPSO and a global aerosol transport model. *Atmospheric*  
715 *Chemistry and Physics*, 9(9), 3137–3145. <https://doi.org/10.5194/acp-9-3137-2009>  
716 Fang, Y., Mauzerall, D. L., Liu, J., Fiore, A. M., & Horowitz, L. W. (2013). Impacts of 21st century climate change  
717 on global air pollution-related premature mortality. *Climatic Change*, 121(2), 239–253.  
718 <https://doi.org/10.1007/s10584-013-0847-8>  
719 Field, P. R., & Wood, R. (2007). Precipitation and cloud structure in midlatitude cyclones. *Journal of Climate*,  
720 20(2), 233–254. <https://doi.org/10.1175/JCLI3998.1>  
721 Gelaro, R., McCarty, W., Suárez, M. J., Todling, R., Molod, A., Takacs, L., ... Zhao, B. (2017). The Modern-Era  
722 Retrospective Analysis for Research and Applications, Version 2 (MERRA-2). *Journal of Climate*, 30(14),  
723 5419–5454. <https://doi.org/10.1175/JCLI-D-16-0758.1>  
724 Ginoux, P., Chin, M., Tegen, I., Prospero, J. M., Holben, B., Dubovik, O., & Lin, S.-J. (2001). Sources and  
725 distributions of dust aerosols simulated with the GOCART model. *Journal of Geophysical Research:*  
726 *Atmospheres*, 106(D17), 20255–20273. <https://doi.org/10.1029/2000JD000053>  
727 Gong, S. L. (2003). A parameterization of sea-salt aerosol source function for sub- and super-micron particles.  
728 *Global Biogeochemical Cycles*, 17(4), 1–7. <https://doi.org/10.1029/2003gb002079>

729 Graedel, T. E., & Weschler, C. J. (1981). Chemistry within aqueous atmospheric aerosols and raindrops. In *Reviews*  
730 *of Geophysics* (Vol. 19). <https://doi.org/10.1029/RG019i004p00505>

731 Grandey, B. S., Stier, P., Grainger, R. G., & Wagner, T. M. (2013). The contribution of the strength and structure of  
732 extratropical cyclones to observed cloud-aerosol relationships. *Atmospheric Chemistry and Physics*, *13*(21),  
733 10689–10701. <https://doi.org/10.5194/acp-13-10689-2013>

734 Grandey, B. S., Stier, P., Wagner, T. M., Grainger, R. G., & Hodges, K. I. (2011). The effect of extratropical  
735 cyclones on satellite-retrieved aerosol properties over ocean. *Geophysical Research Letters*, *38*(13), 1–6.  
736 <https://doi.org/10.1029/2011GL047703>

737 Granier, C., Bessagnet, B., Bond, T., D'Angiola, A., van der Gon, H. D., Frost, G. J., ... van Vuuren, D. P. (2011).  
738 Evolution of anthropogenic and biomass burning emissions of air pollutants at global and regional scales  
739 during the 1980-2010 period. *Climatic Change*, *109*(1), 163–190. <https://doi.org/10.1007/s10584-011-0154-1>

740 Guibert, S., Matthias, V., Schulz, M., Bösenberg, J., Eixmann, R., Mattis, I., ... Vaughan, G. (2005). The vertical  
741 distribution of aerosol over Europe - Synthesis of one year of EARLINET aerosol lidar measurements and  
742 aerosol transport modeling with LMDzT-INCA. *Atmospheric Environment*, *39*(16), 2933–2943.  
743 <https://doi.org/10.1016/j.atmosenv.2004.12.046>

744 Hannan, J. R., Fuelberg, H. E., Crawford, J. H., Sachse, G. W., & Blake, D. R. (2003). Role of wave cyclones in  
745 transporting boundary layer air to the free troposphere during the spring 2001 NASA/TRACE-P experiment.  
746 *Journal of Geophysical Research: Atmospheres*, *108*(20), 1–17. <https://doi.org/10.1029/2002jd003105>

747 He, H., Li, C., Loughner, C. P., Li, Z., Krotkov, N. A., Yang, K., ... Dickerson, R. R. (2012). SO<sub>2</sub> over central  
748 China: Measurements, numerical simulations and the tropospheric sulfur budget. *Journal of Geophysical*  
749 *Research Atmospheres*, *117*(3), 1–15. <https://doi.org/10.1029/2011JD016473>

750 Hess, M., Koepke, P., & Schult, I. (1998). Optical Properties of Aerosols and Clouds: The Software Package OPAC.  
751 *Bulletin of the American Meteorological Society*, *79*(5), 831–844. [https://doi.org/10.1175/1520-0477\(1998\)079<0831:OPOAAC>2.0.CO;2](https://doi.org/10.1175/1520-0477(1998)079<0831:OPOAAC>2.0.CO;2)

752

753 Hodzic, A., Kasibhatla, P. S., Jo, D. S., Cappa, C. D., Jimenez, J. L., Madronich, S., & Park, R. J. (2016).  
754 Rethinking the global secondary organic aerosol (SOA) budget: Stronger production, faster removal, shorter  
755 lifetime. *Atmospheric Chemistry and Physics*, *16*(12), 7917–7941. <https://doi.org/10.5194/acp-16-7917-2016>

756 Hoskins, B. J., & Hodges, K. I. (2002). New perspectives on the Northern Hemisphere winter storm tracks. *Journal*  
757 *of the Atmospheric Sciences*, *59*(6), 1041–1061. [https://doi.org/10.1175/1520-0469\(2002\)059<1041:NPOTNH>2.0.CO;2](https://doi.org/10.1175/1520-0469(2002)059<1041:NPOTNH>2.0.CO;2)

758

759 Huang, J., Minnis, P., Chen, B., Huang, Z., Liu, Z., Zhao, Q., ... Ayers, J. K. (2008). Long-range transport and  
760 vertical structure of Asian dust from CALIPSO and surface measurements during PACDEX. *Journal of*  
761 *Geophysical Research Atmospheres*, *113*(23), 1–13. <https://doi.org/10.1029/2008JD010620>

762 Jacobson, M. C., & Hansson, H. (2000). Review of Aerosols ' Science and State of the. *Reviews of*  
763 *Geophysics*, (1998), 267–294. <https://doi.org/10.1029/1998RG000045>

764 Jaeglé, L., Quinn, P. K., Bates, T. S., Alexander, B., & Lin, J. T. (2011). Global distribution of sea salt aerosols:  
765 New constraints from in situ and remote sensing observations. *Atmospheric Chemistry and Physics*, *11*(7),  
766 3137–3157. <https://doi.org/10.5194/acp-11-3137-2011>

767 Jaeglé, L., Wood, R., & Wargan, K. (2017). Multiyear Composite View of Ozone Enhancements and Stratosphere-  
768 to-Troposphere Transport in Dry Intrusions of Northern Hemisphere Extratropical Cyclones. *Journal of*  
769 *Geophysical Research: Atmospheres*, *122*(24), 13,436-13,457. <https://doi.org/10.1002/2017JD027656>

770 Jaffe, D., McKendry, I., Anderson, T., & Price, H. (2003). Six “new” episodes of trans-Pacific transport of air  
771 pollutants. *Atmospheric Environment*, *37*(3), 391–404. [https://doi.org/10.1016/S1352-2310\(02\)00862-2](https://doi.org/10.1016/S1352-2310(02)00862-2)

772 Jickells, T. D., & Spokes, L. J. (2001). Atmospheric iron inputs to the oceans. In *The Biogeochemistry of Iron in*  
773 *Seawater* (pp. 85–121). Wiley.

774 Joos, H., Madonna, E., Witlox, K., Ferrachat, S., Wernli, H., & Lohmann, U. (2017). Effect of anthropogenic  
775 aerosol emissions on precipitation in warm conveyor belts in the western North Pacific in winter - A model  
776 study with ECHAM6-HAM. *Atmospheric Chemistry and Physics*, *17*(10), 6243–6255.  
777 <https://doi.org/10.5194/acp-17-6243-2017>

778 Kerminen, V. M., Lihavainen, H., Komppula, M., Viisanen, Y., & Kulmala, M. (2005). Direct observational  
779 evidence linking atmospheric aerosol formation and cloud droplet activation. *Geophysical Research Letters*,  
780 *32*(14), 1–4. <https://doi.org/10.1029/2005GL023130>

781 Kinne, S., Lohmann, U., Feichter, J., Schulz, M., Timmreck, C., Ghan, S., ... Kaufman, Y. (2003). Monthly  
782 averages of aerosol properties: A global comparison among models, satellite data, and AERONET ground  
783 data. *Journal of Geophysical Research Atmospheres*, *108*(20). <https://doi.org/10.1029/2001JD001253>

784 Knowland, K. E., Doherty, R. M., & Hodges, K. I. (2015). The effects of springtime mid-latitude storms on trace gas

785 composition determined from the MACC reanalysis. *Atmospheric Chemistry and Physics*, 15(6), 3605–3628.  
786 <https://doi.org/10.5194/acp-15-3605-2015>

787 Larson, E. J. L., & Portmann, R. W. (2019). Anthropogenic aerosol drives uncertainty in future climate mitigation  
788 efforts. *Scientific Reports*, 9(1), 1–8. <https://doi.org/10.1038/s41598-019-52901-3>

789 Levy, R. C., Mattoo, S., Munchak, L. A., Remer, L. A., Sayer, A. M., Patadia, F., & Hsu, N. C. (2013). The  
790 Collection 6 MODIS aerosol products over land and ocean. *Atmospheric Measurement Techniques*, 6(11),  
791 2989–3034. <https://doi.org/10.5194/amt-6-2989-2013>

792 Levy, Robert C., Remer, L. A., Tanré, D., Kaufman, Y. J., Ichoku, C., Holben, B. N., ... Maring, H. (2003).  
793 Evaluation of the moderate-resolution imaging spectroradiometer (MODIS) retrievals of dust aerosol over the  
794 ocean during PRIDE. *Journal of Geophysical Research: Atmospheres*, 108(19), 1–13.  
795 <https://doi.org/10.1029/2002jd002460>

796 Liang, Q., Jaeglé, L., Jaffe, D. A., Weiss-Penzias, P., Heckman, A., & Snow, J. A. (2004). Long-range transport of  
797 Asian pollution to the northeast Pacific: Seasonal variations and transport pathways of carbon monoxide.  
798 *Journal of Geophysical Research D: Atmospheres*, 109(23), 1–16. <https://doi.org/10.1029/2003JD004402>

799 Luan, Y., & Jaeglé, L. (2013). Composite study of aerosol export events from East Asia and North America.  
800 *Atmospheric Chemistry and Physics*, 13(3), 1221–1242. <https://doi.org/10.5194/acp-13-1221-2013>

801 McCarty, W., Coy, L., Gelaro, R., Huang, A., Merkova, D., Smith, E.B., Sienkiewicz, M., Wargan, K. (2016).  
802 MERRA-2 input observations: Summary and assessment. *NASA/TM-2016-104606*, 46, 64.

803 McCoy, D. T., Field, P. R., Schmidt, A., Grosvenor, D. P., Bender, F. A. M., Shipway, B. J., ... Elsaesser, G. S.  
804 (2018). Aerosol midlatitude cyclone indirect effects in observations and high-resolution simulations.  
805 *Atmospheric Chemistry and Physics*, 18(8), 5821–5846. <https://doi.org/10.5194/acp-18-5821-2018>

806 Molod, A., Takacs, L., Suarez, M., & Bacmeister, J. (2015). Development of the GEOS-5 atmospheric general  
807 circulation model: Evolution from MERRA to MERRA2. *Geoscientific Model Development*, 8(5), 1339–1356.  
808 <https://doi.org/10.5194/gmd-8-1339-2015>

809 Naud, C. M., Booth, J. F., Jeyaratnam, J., Donner, L. J., Seman, C. J., Zhao, M., ... Ming, Y. (2019). Extratropical  
810 cyclone clouds in the GFDL climate model: Diagnosing biases and the associated causes. *Journal of Climate*,  
811 32(20), 6685–6701. <https://doi.org/10.1175/JCLI-D-19-0421.1>

812 Naud, C. M., Posselt, D. J., & van den Heever, S. C. (2016). Aerosol optical depth distribution in extratropical  
813 cyclones over the Northern Hemisphere oceans. *Geophysical Research Letters*, 43(19), 10,504–10,511.  
814 <https://doi.org/10.1002/2016GL070953>

815 Naud, C. M., Posselt, D. J., & van den Heever, S. C. (2017). Observed Covariations of Aerosol Optical Depth and  
816 Cloud Cover in Extratropical Cyclones. *Journal of Geophysical Research: Atmospheres*, 122(19), 10,338–  
817 10,356. <https://doi.org/10.1002/2017JD027240>

818 Nielsen, J. E., Pawson, S., Molod, A., Auer, B., da Silva, A. M., Douglass, A. R., ... Wargan, K. (2017). Chemical  
819 Mechanisms and Their Applications in the Goddard Earth Observing System (GEOS) Earth System Model.  
820 *Journal of Advances in Modeling Earth Systems*, 9(8), 3019–3044. <https://doi.org/10.1002/2017MS001011>

821 Nowotnick, E., Colarco, P., Ferrare, R., Chen, G., Ismail, S., Anderson, B., & Browell, E. (2010). Online  
822 simulations of mineral dust aerosol distributions: Comparisons to namma observations and sensitivity to dust  
823 emission parameterization. *Journal of Geophysical Research Atmospheres*, 115(3), 1–19.  
824 <https://doi.org/10.1029/2009JD012692>

825 Orbe, C., Oman, L. D., Strahan, S. E., Waugh, D. W., Pawson, S., Takacs, L. L., & Molod, A. M. (2017). Large-  
826 Scale Atmospheric Transport in GEOS Replay Simulations. *Journal of Advances in Modeling Earth Systems*,  
827 9(7), 2545–2560. <https://doi.org/10.1002/2017MS001053>

828 Park, R. J., Jacob, D. J., Palmer, P. I., Clarke, A. D., Weber, R. J., Zondlo, M. A., ... Bond, T. C. (2005). Export  
829 efficiency of black carbon aerosol in continental outflow: Global implications. *Journal of Geophysical  
830 Research D: Atmospheres*, 110(11), 1–7. <https://doi.org/10.1029/2004JD005432>

831 Partanen, A. I., Landry, J. S., & Matthews, H. D. (2018). Climate and health implications of future aerosol emission  
832 scenarios. *Environmental Research Letters*, 13(2). <https://doi.org/10.1088/1748-9326/aaa511>

833 Patoux, J., Yuan, X., & Li, C. (2009). Satellite-based midlatitude cyclone statistics over the Southern Ocean: 1.  
834 Scatterometer-derived pressure fields and storm tracking. *Journal of Geophysical Research*, 114(D4).  
835 <https://doi.org/10.1029/2008JD010873>

836 Platnick, S., King, M. D., Meyer, K. G., Wind, G., Amarasinghje, N., Marchant, B., ... Riedi, J. (2015). *MODIS  
837 Cloud Optical Properties : User Guide for the Collection 6 Level-2 MOD06 / MYD06 Product and Associated  
838 Level-3 Datasets*. Retrieved from [https://atmosphere-  
839 imager.gsfc.nasa.gov/sites/default/files/ModAtmo/C6MOD06OPUserGuide\\_0.pdf](https://atmosphere-imager.gsfc.nasa.gov/sites/default/files/ModAtmo/C6MOD06OPUserGuide_0.pdf)

840 Prather, K. A., Hatch, C. D., & Grassian, V. H. (2008). Analysis of atmospheric aerosols. *Annual Review of*

841 *Analytical Chemistry*, 1(1), 485–514. <https://doi.org/10.1146/annurev.anchem.1.031207.113030>

842 Randles, C. A., da Silva, A. M., Buchard, V., Colarco, P. R., Darmenov, A., Govindaraju, R., ... Flynn, C. J. (2017).

843 The MERRA-2 aerosol reanalysis, 1980 onward. Part I: System description and data assimilation evaluation.

844 *Journal of Climate*, 30(17), 6823–6850. <https://doi.org/10.1175/JCLI-D-16-0609.1>

845 Real, E., Pissò, I., Law, K. S., Legras, B., Bousseres, N., Schlager, H., ... Attié, J. L. (2010). Toward a novel high-

846 resolution modeling approach for the study of chemical evolution of pollutant plumes during long-range

847 transport. *Journal of Geophysical Research Atmospheres*, 115(12), 1–14.

848 <https://doi.org/10.1029/2009JD011707>

849 Remer, A. L., Kaufman, Y. J., Tanré, D., Mattoo, S., Chu, D. A., ... and B N Holben. (2005). The MODIS Aerosol

850 Algorithm, Products, and Validation. *Journal of the Atmospheric Sciences*, 62(4), 947–973.

851 Remer, L. A., Kleidman, R. G., Levy, R. C., Kaufman, Y. J., Tanré, D., Mattoo, S., ... Holben, B. N. (2008). Global

852 aerosol climatology from the MODIS satellite sensors. *Journal of Geophysical Research Atmospheres*,

853 113(14), 1–18. <https://doi.org/10.1029/2007JD009661>

854 Shindell, D. T., Lamarque, J. F., Schulz, M., Flanner, M., Jiao, C., Chin, M., ... Lo, F. (2013). Radiative forcing in

855 the ACCMIP historical and future climate simulations. *Atmospheric Chemistry and Physics*, 13(6), 2939–

856 2974. <https://doi.org/10.5194/acp-13-2939-2013>

857 Silva, R. A., West, J. J., Lamarque, J. F., Shindell, D. T., Collins, W. J., Faluvegi, G., ... Zeng, G. (2017). Future

858 global mortality from changes in air pollution attributable to climate change. *Nature Climate Change*, 7(9),

859 647–651. <https://doi.org/10.1038/nclimate3354>

860 Simpson, I. R., Shaw, T. A., & Seager, R. (2014). A diagnosis of the seasonally and longitudinally varying

861 midlatitude circulation response to global warming. *Journal of the Atmospheric Sciences*, 71(7), 2489–2515.

862 <https://doi.org/10.1175/JAS-D-13-0325.1>

863 Sinclair, V. A., Gray, S. L., & Belcher, S. E. (2008). Boundary-layer ventilation by baroclinic life cycles. *Quarterly*

864 *Journal of the Royal Meteorological Society*, 134(635), 1409–1424. <https://doi.org/10.1002/qj.293>

865 Smith, S. J., & Bond, T. C. (2014). Two hundred fifty years of aerosols and climate: The end of the age of aerosols.

866 *Atmospheric Chemistry and Physics*, 14(2), 537–549. <https://doi.org/10.5194/acp-14-537-2014>

867 Stohl, A. (2001). A 1-year Lagrangian “climatology” of airstreams in the Northern Hemisphere troposphere and

868 lowermost stratosphere. *Journal of Geophysical Research Atmospheres*, 106(D7), 7263–7279.

869 <https://doi.org/10.1029/2000JD900570>

870 Strahan, S. E., Duncan, B. N., & Hoor, P. (2007). Observationally derived transport diagnostics for the lowermost

871 stratosphere and their application to the GMI chemistry and transport model. *Atmospheric Chemistry and*

872 *Physics*, 7(9), 2435–2445. <https://doi.org/10.5194/acp-7-2435-2007>

873 Strode, S. A., Ziemke, J. R., Oman, L. D., Lamsal, L. N., Olsen, M. A., & Liu, J. (2019). Global changes in the

874 diurnal cycle of surface ozone. *Atmospheric Environment*, 199(August 2018), 323–333.

875 <https://doi.org/10.1016/j.atmosenv.2018.11.028>

876 Szopa, S., V. Naik, B. Adhikary, P. Artaxo, T. Berntsen, W.D. Collins, S. Fuzzi, L. Gallardo, A. Kiendler-Scharr,

877 Z. Klimont, H. Liao, N. Unger, and P. Zanis, 2021: Short-Lived Climate Forcers. In *Climate Change 2021:*

878 *The Physical Science Basis. Contribution of Working Group I to the Sixth Assessment Report of the*

879 *Intergovernmental Panel on Climate Change* [Masson-Delmotte, V., P. Zhai, A. Pirani, S.L. Connors,

880 C. Péan, S. Berger, N. Caud, Y. Chen, L. Goldfarb, M.I. Gomis, M. Huang, K. Leitzell, E. Lonnoy,

881 J.B.R. Matthews, T.K. Maycock, T. Waterfield, O. Yelekçi, R. Yu, and B. Zhou (eds.)]. Cambridge University

882 Press, Cambridge, United Kingdom and New York, NY, USA, pp. 817–922, doi:10.1017/9781009157896.008

883 Turnock, S. T., Allen, R. J., Andrews, M., Bauer, S. E., Deushi, M., Emmons, L., ... Zhang, J. (2020). Historical and

884 future changes in air pollutants from CMIP6 models. *Atmospheric Chemistry and Physics*, 20(23), 14547–

885 14579. <https://doi.org/10.5194/acp-20-14547-2020>

886 Ulbrich, U., Leckebusch, G. C., & Pinto, J. G. (2009). *Extra-tropical cyclones in the present and future climate : a*

887 *review*. 117–131. <https://doi.org/10.1007/s00704-008-0083-8>

888 Wang, Y., Zhang, R., & Saravanan, R. (2014). Asian pollution climatically modulates mid-latitude cyclones

889 following hierarchical modelling and observational analysis. *Nature Communications*, 5.

890 <https://doi.org/10.1038/ncomms4098>

891 Wei, J., Li, Z., Peng, Y., & Sun, L. (2019a). MODIS Collection 6.1 aerosol optical depth products over land and

892 ocean: validation and comparison. *Atmospheric Environment*, 201(October 2018), 428–440.

893 <https://doi.org/10.1016/j.atmosenv.2018.12.004>

894 Wei, J., Peng, Y., Guo, J., & Sun, L. (2019b). Performance of MODIS Collection 6.1 Level 3 aerosol products in

895 spatial-temporal variations over land. *Atmospheric Environment*, 206(September 2018), 30–44.

896 <https://doi.org/10.1016/j.atmosenv.2019.03.001>

897 Weng, H., Lin, J., Martin, R., Millet, D. B., Jaeglé, L., Ridley, D., ... Meng, J. (2020). Global high-resolution  
898 emissions of soil NO<sub>x</sub>, sea salt aerosols, and biogenic volatile organic compounds. *Scientific Data*, 7(1), 1–15.  
899 <https://doi.org/10.1038/s41597-020-0488-5>

900 Wernli, H., & Schwierz, C. (2006). Surface cyclones in the ERA-40 dataset (1958-2001). Part I: Novel identification  
901 method and global climatology. *Journal of the Atmospheric Sciences*, 63(10), 2486–2507.  
902 <https://doi.org/10.1175/JAS3766.1>

903 Westervelt, D. M., Horowitz, L. W., Naik, V., Golaz, J. C., & Mauzerall, D. L. (2015). Radiative forcing and  
904 climate response to projected 21st century aerosol decreases. *Atmospheric Chemistry and Physics*, 15(22),  
905 12681–12703. <https://doi.org/10.5194/acp-15-12681-2015>

906 Whitaker, J. S., Uccellini, L. W., & Brill, K. F. (1988). A Model-Based Diagnostic Study of the Rapid Development  
907 Phase of the Presidents's Day Cyclone. *Monthly Weather Review*, 116(11), 2337–2365.  
908 [https://doi.org/10.1175/1520-0493\(1988\)116<2337:AMBDSO>2.0.CO;2](https://doi.org/10.1175/1520-0493(1988)116<2337:AMBDSO>2.0.CO;2)

909 Yang, Q., Easter, R. C., Campuzano-Jost, P., Jimenez, J. L., Fast, J. D., Ghan, S. J., ... Wisthaler, A. (2015). Aerosol  
910 transport and wet scavenging in deep convective clouds: A case study and model evaluation using a multiple  
911 passive tracer analysis approach. *Journal of Geophysical Research: Atmospheres*, 120(16), 8448–8468.  
912 <https://doi.org/10.1002/2015JD023647>

913 Yang, Y., Liao, H., & Lou, S. (2015). Decadal trend and interannual variation of outflow of aerosols from East Asia:  
914 Roles of variations in meteorological parameters and emissions. *Atmospheric Environment*, 100, 141–153.  
915 <https://doi.org/10.1016/j.atmosenv.2014.11.004>

916 Yu, H., Remer, L. A., Chin, M., Bian, H., Kleidman, R. G., & Diehl, T. (2008). A satellite-based assessment of  
917 transpacific transport of pollution aerosol. *Journal of Geophysical Research*, 113(D14), 1–15.  
918 <https://doi.org/10.1029/2007jd009349>

919 Zhang, R., Li, G., Fan, J., Wu, D. L., & Molina, M. J. (2007). Intensification of Pacific storm track linked to Asian  
920 pollution. *Proceedings of the National Academy of Sciences of the United States of America*, 104(13), 5295–  
921 5299. <https://doi.org/10.1073/pnas.0700618104>

922